



Structures and electronic properties of functional molecules on metal substrates: From single molecule to self-assemblies

Lei Tao¹ | Yu-yang Zhang^{1,2}  | Shixuan Du^{1,2,3,4} 

¹Institute of Physics and University of Chinese Academy of Sciences, Chinese Academy of Sciences, Beijing, China

²CAS Center for Excellence in Topological Quantum Computation, Beijing, China

³Beijing National Laboratory for Condensed Matter Physics, Beijing, China

⁴Songshan Lake Materials Laboratory, Dongguan, China

Correspondence

Shixuan Du, Institute of Physics and University of Chinese Academy of Sciences, Chinese Academy of Sciences, Beijing 100190, China.
Email: sxdu@iphy.ac.cn

Funding information

This work was supported by grants from the National Natural Science Foundation of China (61888102), National Key Research and Development Projects of China (2016YFA0202300), the Strategic Priority Research Program of the Chinese Academy of Sciences (XDB30000000), and the Fundamental Research Funds for the Central Universities.

Edited by: Jinlong Yang, Associate Editor

Abstract

Functional molecules and their assemblies have attracted considerable attention arising from not only diverse structures with novel properties but also potential applications in molecular devices. The novel properties, which determine their applications, are strongly related to their structures. In recent years, benefiting from the development of atomically precise control technique of the structures, a lot of new materials constructing from molecules with novel properties emerged. Their novel properties enable them to be potentially applied in molecular spintronics, high-density data storage, selective reaction and quantum topological devices, and so on. The present review focuses on new progress in predicting and controlling the structures and properties of functional molecules and their assemblies on metal surfaces by combining first-principle calculations with scanning tunneling microscopy experiments. We aim at understanding the key factors which affect the physical and chemical properties of the metal–organic systems, especially from a theoretical perspective.

This article is categorized under:

Structure and Mechanism > Molecular Structures

Electronic Structure Theory > Density Functional Theory

KEYWORDS

functional molecules, molecular spintronics, quantum topological devices, selective reaction, self-assembly

1 | INTRODUCTION

Constructing low-dimensional supramolecular structures by self-assembly of organic molecules is a simple and effective method commonly used in surface sciences.^{1,2} The constructed structures have various physical and chemical properties, such as high carrier mobility,^{3,4} photoactive dielectric property,⁵ photoconductive property,^{6,7} magnetic anisotropy,⁸ ferroelectricity,^{9–11} and piezoelectricity.^{12,13} Because the low-dimensional supramolecular structures are easily processable, flexible, energy friendly, cheap, and compatible with other nano-devices, they show potential applications in field-effect transistors,^{14–16} sensors,^{17–20} drug delivery,²¹ nonlinear optics,^{22,23} batteries,²⁴ electrocatalysts,²⁵ heterogeneous catalysts, photocatalysts,^{25,26} and so on.

The self-assembly of organic molecules on a metal surface is a process of association of individual molecules into highly ordered structures, which are closely related to a balance between the molecule–molecule interaction and molecule–surface interaction. The main types of interactions involved in the self-assembly of organic molecules on surfaces include covalent bonds,²⁷ coordination bonds,²⁸ hydrogen and fluorine/halogen bonds,^{29,30} and other weak van der Waals interactions.³¹ Usually, the strength of coordinated bond and covalent bond is from 200 to 1000 kJ/mol.³² The hydrogen bond and vdWs interaction are much weaker, in which the energy is about 12–30 kJ/mol for hydrogen bond, and 0.4–4.0 kJ/mol for van der Waals interaction. By changing the configuration and composition of precursors, the supramolecular structure with specific structures and properties has been fabricated through self-assembly strategy on metal surfaces.^{33–35} Further control of the structures and properties of organic molecules and their self-assemblies, which can be achieved by applying an external electric or magnetic field,^{36–38} optical technique,^{39,40} and mechanical manipulation using scanning probe microscope tips,^{41–43} provides opportunities to realize the functionalization of low-dimensional materials at the atomic level.

First-principle density functional theory (DFT) is widely used in low-dimensional supramolecular structures on surface. Considering different interactions in metal–organic systems, selection of exchange–correlation functionals and van der Waals corrections is very important to correctly describe the geometric and electronic properties. Local density approximation (LDA) and generalized gradient approximation (GGA) are commonly used to give good descriptions of molecular geometry. Hybrid functionals such as Heyd–Scuseria–Ernzerhof (HSE),^{44–46} Becke-3-parameter-Lee–Yang–Parr (B3LYP),⁴⁷ and Perdew–Burke–Ernzerhof (PBE0)⁴⁸ can provide reasonable orbital order and electronic structures of molecules. Van der Waals corrections, including dispersion-corrected density functional (DFT-D)^{49,50} and van der Waals density functional (vdW-DF),^{51,52} can be used to improve the description of the dispersion force in molecule–metal systems. However, the performance of functionals depends critically on whether the functional fit with the physical properties of calculated system. To give better description on metal–organic interactions and get reasonable results, the exchange–correlation functionals and van der Waals corrections need to be customized in different systems.

Although many efforts have been devoted by both theoretical investigations and experimental analysis, a review from a theoretical aspect of theoretical and experimental progresses on structures, electronic properties, possible applications and their relationships of functional molecules on metal substrates is still lacking. To facilitate the application of functional molecules and their assemblies, it is important to review recent developments and understand the key issues which affect the properties and applications. Therefore, we review the construction and novel properties of functional molecules on surfaces and their potential applications in molecular electronics, chemical synthesis, quantum topological devices, and so on. In the meantime, we also provide theoretical insights for the manipulations of self-assembly and further applications. First, we discuss the reversible spin control of metal phthalocyanine (MPc) molecules and their assemblies and their applications in molecular spintronics and high-density data storage. Then we introduce the enhanced selectivity in both intermolecular and intramolecular reactions through self-assembly strategy in on-surface synthesis. Finally, we discuss the prediction of metal–organic molecular networks that exhibit quantum topological states and superconductivity.

2 | HIGH-DENSITY STORAGE BASED ON SINGLE MOLECULES AND SELF-ASSEMBLIES

Until 2020, the size of a bit-cell of static random-access memory is down to 0.02 μm^2 and the transistor density is 100 million per mm^2 ,⁵³ which has approached the limit of traditional fabrication technique. In order to meet the requirement of the further miniaturization of electronic devices, nano-devices based on functional molecules have attracted much attention. Moreover, the self-assembly of functional molecules with highly ordered structures provides a simple and efficient way to fabricate high-density arrays. For example, magnetic MPc molecules have been reported to exhibit controllable spin states at the metal centers and can be used as building blocks of molecule-based high-density storage. Considering the size of a MPc molecule is $\sim 1 \text{ nm}^2$, the density of a memory device based on the molecular arrays can be 1000 billion per mm^2 . Therefore, constructing the self-assembly of functional molecules and controlling their configurations to realize the reading and writing function at the atomic level are of great significance in high-density data storage.

The design of data storage device based on ON/OFF spin states of magnetic molecules relies on the accuracy of theoretical calculations of atomic and spin configurations of the host molecules. DFT calculations using the standard GGA can provide reasonable descriptions of adsorbate configurations on metal surfaces, but may be insufficient to accurately

describe the weak vdW interactions. For example, although PW91 or PBE functionals correctly describe the adsorption configurations of pyridine on Au(111), the adsorption energies are underestimated.⁵⁴ Depending on whether the weak vdW forces have significant influence on the spin properties of molecule, the researchers should be careful to choose the vdW functionals. The spin-polarized calculation can predict the magnetism with the approximation like local spin density approximation (LSDA) and GGA. Furthermore, hybrid functionals usually give better description on the magnetic properties of molecules than LSDA and GGA. Similarly, DFT+U method by treating the strong on-site Coulomb interaction of localized electrons on the atom can also give a good description on the magnetic properties.⁵⁵ By changing the Hubbard U parameters, DFT+U method can reproduce the result of hybrid functionals, but cost significantly less time than hybrid functional calculation. Considering computational efficiency, it is important to make the appropriate choice of method to get the accurate atomic and spin configurations of self-assemblies.

2.1 | Self-assembly behaviors of MPc on Au(111) surface

The self-assembly process is controlled both by the molecule–molecule interaction and molecule–surface interaction. When the molecule–surface interaction plays a major role, the molecular self-assembly structure is mainly determined by the properties of surfaces.^{56–58} When the molecule–molecule interaction is stronger than the molecule–surface interaction, the self-assembled pattern is determined by the interaction between the molecules rather than the morphology of surfaces.^{59–61} For example, according to the morphology of surfaces, iron phthalocyanine (FePc) exhibits different adsorption behaviors on graphene,^{62,63} Au(111),^{64,65} Au(110),⁶⁶ Ag(111),⁶⁶ TiO₂(110),⁶⁷ and so forth. The adsorption of molecule and the assemblies can even induce surface reconstruction.⁶⁸

MPc consists of a central metal atom and a π -conjugated organic framework. Due to various applications on light-emitting diodes,⁶⁹ photovoltaic cells,⁷⁰ single-molecule rotors,⁷¹ and single-molecular devices,⁷² MPc molecule becomes a model system for surface science and nanotechnology.^{73–75} Thus, understanding the self-assembled patterns of MPc molecules on different surfaces will provide useful information for other systems of molecules on surfaces.

First-principle calculations found that FePc, CoPc, and MnPc have a stronger binding configuration than that of NiPc, CuPc, and ZnPc on Au(111) surface,⁶⁵ indicating the strength of molecule–molecule interaction and molecule–surface interaction is different in these two groups of molecules. Experiments found that CoPc,⁷⁶ FePc,⁷⁷ and MnPc⁷⁸ adsorbed on Au(111) dispersedly due to the strong binding to the surface while ZnPc and its derivatives adsorbed on Au(111) as monolayer clusters at low coverages,⁷⁹ showing excellent agreement with theoretical predictions.

For FePc on Au(111), at ~ 0.01 monolayer (ML) coverage, FePc molecules are located at step edge, constructing one-dimensional molecular chains,⁸⁰ as showing in Figure 1a. The atomic configuration in Figure 1e shows that, there are three FePc molecules adsorbed on a monatomic step edge in face-centered cubic (fcc) regions on Au(111). The iron ion is clearly resolved in the STM image in Figure 1a, and two lobes are on the upper terrace with the other two on the lower terrace.⁸⁰ The calculated binding energy for FePc at step edge is higher than other configurations, which means that the edge of fcc step is more active than other sites for FePc adsorption.

As the coverage increased, all step edges are occupied by FePc molecules. Then FePc molecules are adsorbed on the fcc regions of the reconstructed Au(111) surface at the coverage of ~ 0.1 ML (Figure 1b). Meanwhile, there is almost no molecule on the hexagonal close packing (hcp) regions, while an individual molecule is at the elbow site of the hcp regions. The reason is that, the electronic potential energies of these elbow sites are higher than those of the fcc and hcp regions. Besides, various molecules have been found to have similar behaviors.^{81,82} Because the adsorption of FePc molecules on the fcc regions is more stable than those on the hcp regions, the FePc molecules prefer to adsorb on the fcc regions. Therefore, the strength of interaction between MPc molecules and the Au(111) decreases from elbow sites to fcc and hcp regions.⁸³

The authors also notice that there are two stable adsorption configurations (I and II) with different orientations, marked in Figure 1b by arrows. The energy difference is 91 meV according to DFT calculations.⁶⁵ For configuration I (Figure 1f), the iron ion locates at the bridge site of Au(111). For configuration II, the iron ion locates at the atop site and the rotation angle of “cross” is 15° compared to configuration I.⁸⁴

At the coverage of 0.3 ML, the FePc molecules start to adsorb on hcp regions.⁶⁴ At this coverage, the FePc molecules on hcp regions distribute individually, while the FePc on fcc regions are densely packed. Moreover, the MPc molecules form dimers and trimers at the elbow sites. The directional attractive intermolecular interaction indicates that, there is electrostatic interaction between the nitrogen atom and the hydrogen atoms of the phenyl group of the neighboring molecule.⁶⁴

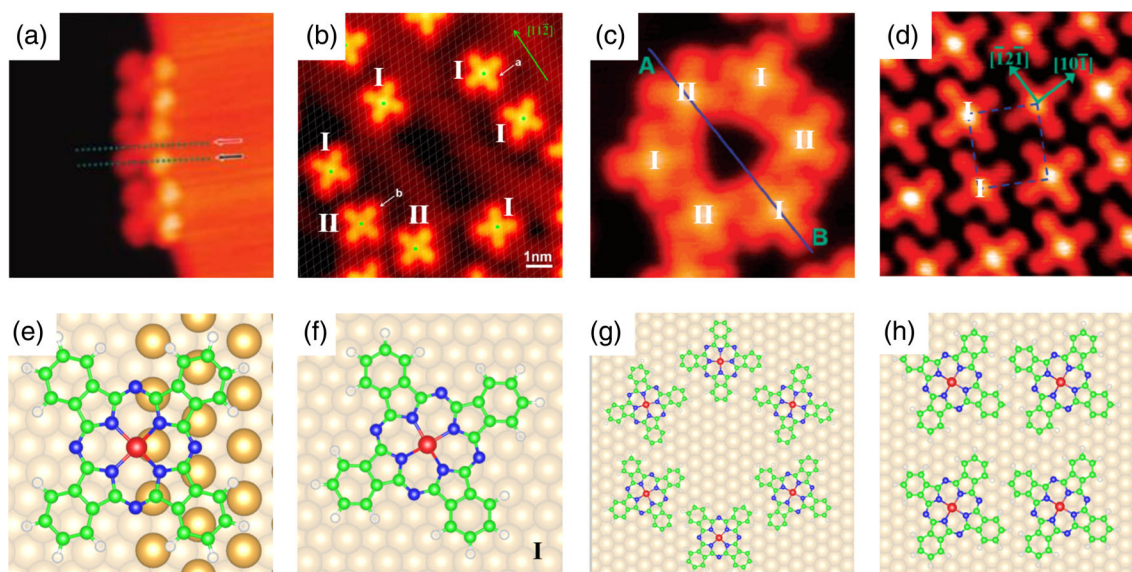


FIGURE 1 Adsorption and self-assembled structure of FePc molecules on Au(111) surface at varying coverages from 0.01 to 2 ML. (a) STM image of FePc selectively decorating the step edges of Au(111) at very low coverage (~ 0.01 ML).⁸⁰ (e) The atomic structure of (a). (b) STM image of FePc on Au(111) at coverage of 0.1 ML. There are two adsorption configurations of FePc, marked by I and II.⁸⁴ (f) The atomic structure of configuration I. The structure of configuration II is the molecule rotated $\sim 15^\circ$ compared to configuration I. (c) STM images of FePc on Au(111) at coverage of 0.6 ML.⁶⁴ (g) The atomic structure of FePc hexamers in (c). (d) STM image of FePc on Au(111) at coverage of 1 ML.⁷⁷ (h) The atomic structure of the unit cell in (d). In (e), (f), (g), and (h), the original data are re-plotted

At the coverage of ~ 0.6 ML, the FePc molecules arranged into lines along the domain walls.⁶⁴ In Figure 1c,g, there is a hexamer with a central hole at elbow sites. All the hexamers have a similar structure and orientation. Note that each molecule in configuration II interacts with its neighboring molecules in configuration I, where the phenyl groups fit with the hollow sites of the neighboring molecules,⁶⁴ as shown in Figure 1g.

At the saturated coverage of 1 ML (Figure 1d), FePc molecules form a well-ordered monolayer structure, in which all molecules are configuration I (Figure 1h). It is different from the two configurations at the submonolayer coverage. Thus, as the coverage increases, the intermolecular interaction plays more important role than molecule-metal surface interaction. When there are two layers of FePc, the unit cell of the second layer shifts compared with the unit cell of the first layer.⁷⁷

2.2 | Configurations and spin states in MPc on Au(111)

The spin states of MPc molecules are of crucial importance in the fabrication of molecular electronics or spintronics.^{85–87} The magnetic properties of MPcs depend basically on the configuration and electronic ground state of the metal substitution. For a single MPc molecule, it was found that the LDA/PBE has been shown to generate very good atomic geometries, while a hybrid functional such as the HSE03 and PBE0, successfully canceled the self-interaction errors.^{88,89} However, for MPc-metal interfaces, things are more complicated. It is found that LDA and PW91 functional give different atomic structures and magnetic properties in FePc/Au(111) system.^{74,84,90} It was also found that the non-local vdW-DF functional, which fails in many aromatic-molecule/Cu(111) system, gives a good description in FePc/Au(111) and CoPc/Au(111).^{91–93} DFT calculations show that there are several molecular adsorption configurations of MPc on Au(111) substrate.⁶⁵ For MnPc, FePc, CoPc, and NiPc, the most stable adsorption site is the atop site (configuration I in Figure 2a). For CuPc and ZnPc, it is hcp and bridge site, respectively. NiPc and ZnPc are non-spin polarized.⁶⁵ The magnetic moment is 1 μB for CuPc, 2 μB for FePc, and 3 μB for MnPc. For CoPc, the magnetic moment of a single molecule is 1 μB . After adsorption, the spin moment is much less than that of a single molecule.^{65,94}

The experimental results agree with the theoretical calculations. For FePc on Au(111) at low coverage, configurations I and II (Figure 2a,c) have the lowest and the second lowest binding energy, respectively. For the two configurations, there is a slight energy shift of *d*-orbitals near the Fermi level,⁸⁴ but the spin-electron coupling of I and II is quite

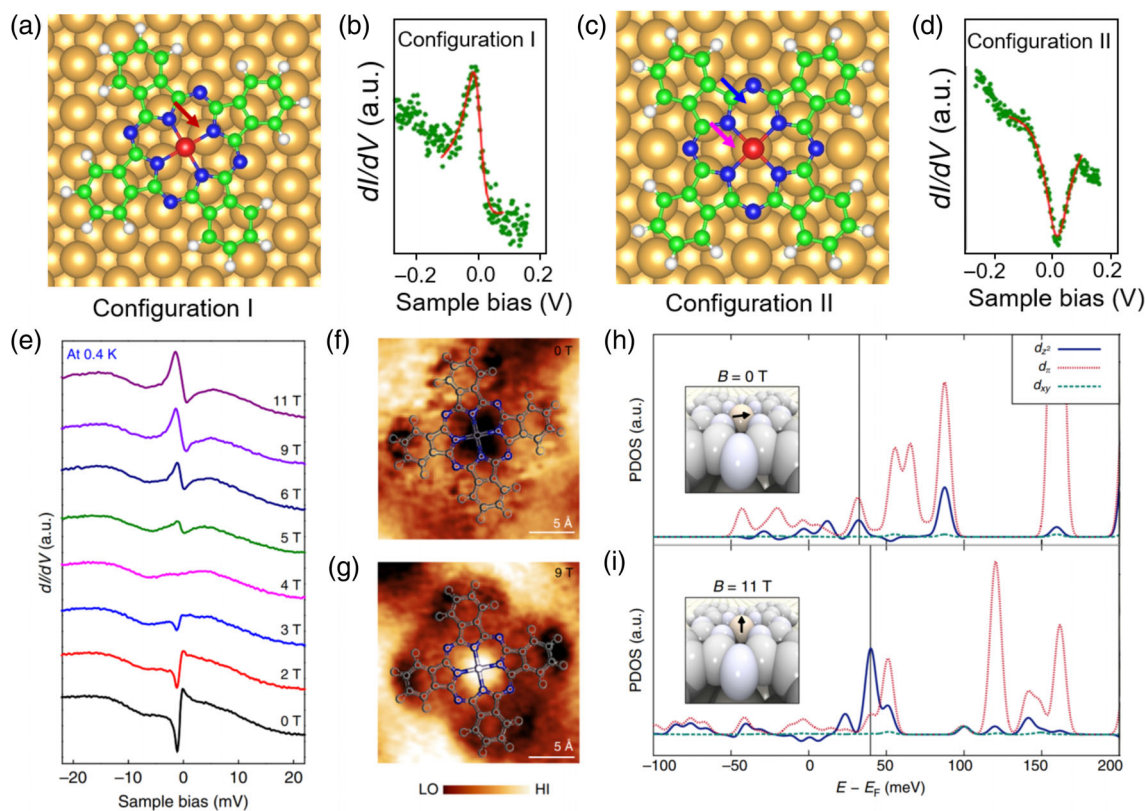


FIGURE 2 Kondo effect of FePc on Au(111) tuned by adsorption sites and external electric field. (a,c) Atomic configuration of FePc adsorbed at (a) bridge site and (d) atop site.⁸⁴ (b,d) dI/dV spectra measured at the molecular center in different adsorption sites in (a) and (d), respectively.⁸⁴ (e) Evolution of the dI/dV spectra of configuration I with increasing magnetic field at 0.4 K, showing a dip-to-peak transition.¹⁰¹ (f,g) dI/dV mapping taken around the Fermi energy at 0 and 9 T, respectively.¹⁰¹ (h,i) Calculated lm -decomposed partial density of states (PDOS) of the d_{xy} , d_{xz} , and d_z^2 bands of Fe atom with a magnetization vector (h) in the plane of the molecule, and (i) in the direction of the magnetic field, which is perpendicular to the plane of the molecule. The arrows in the insets show the direction of the magnetic moment¹⁰¹

different. There is a nonvanishing magnetic moment on the Au atom under the iron atom in configuration II, while the Au atom in configuration I is non-spin polarized.⁸⁴ Therefore, the configuration II has much stronger Fe–Au interaction and a much higher Kondo temperature than that in configuration I. At the ground state, both the d_z^2 and d_{xz}/d_{yz} orbitals are closed to the Fermi level. The electronic density of states near the Fermi surface under a weak magnetic field is mainly contributed by d_{xz}/d_{yz} orbital, while it is mainly contributed by the d_z^2 orbital with a strong magnetic field (Figure 2h,i).

Using scanning tunneling microscopes, the magnetic properties of transition metal ions in a molecule can be verified by a Kondo resonance,^{95,96} which is induced by the interaction between the molecular localized spin electron and the conduction electrons in the metal substrate.^{76,97,98} For FePc on Au(111), there is a site-specific Kondo effect, in which the signal of Kondo resonance depends strongly on the adsorption site.⁸⁴ Differential conductance (dI/dV) spectra measured at the molecular center, which indicates that the peak and dip are from the magnetic atom.⁸⁴ The dI/dV spectra have a narrow peak for configuration I (Figure 2b), but a narrow dip for configuration II (Figure 2d).⁸⁴

The tunneling channels can be also controlled by external magnetic field.^{99,100} The Kondo resonance appeared at the Fermi level changes from valley to peak with the increase of the magnetic field from 0 to 11 T, as shown in Figure 2e.¹⁰¹ Further mapping of the Kondo resonance signal at the Fermi surface with no magnetic field in Figure 2f and magnetic field of 9 T in Figure 2g show that, when the magnetic field is not applied, the Kondo resonance is asymmetrically distributed in the real space, while it is symmetric with the magnetic field of 9 T. DFT calculation shows that, the intensity of applied magnetic field influences the orientation of magnetic moment in FePc. As the magnetic field increases, the transmission path of electrons gradually changes from d_{xz}/d_{yz} to d_z^2 . They also realized the control of a giant magnetoresistance effect, and obtained the change in molecular conductance up to 93%.

Similar to FePc, other magnetic MPc molecule, such as MnPc, also has Kondo resonance on Au(111),^{78,96} Ag(001),¹⁰² and Pb(111).^{103–105} Moreover, NiPc molecule, in which a single molecule has no spin moment, exists a delocalized Kondo effect after adsorption on Ag(100) due to the electron transfer between NiPc and Ag(100).^{106,107}

2.3 | Controlling the configurations and spin states

Controlling spin state is important for the applications. The spin states of MPc can be tuned by dehydrogenation of the organic frameworks.^{94,96} The spin moment of a free CoPc molecule is 1 μ_B , and is reduced due to the adsorption on Au(111).⁶⁵ Therefore, there is no Kondo effect after adsorption on Au(111) because the Co ions do not interact strongly with conduction electrons.^{76,94} After dehydrogenation of the ligand, the calculated magnetic moment of the artificial structure is 1.03 μ_B , similar to the magnetism in a free CoPc molecule. In experiment, after dehydrogenation by voltage pulses using a STM tip,⁹⁴ the Kondo effect is recovered. Similarly, after the dehydrogenation of MnPc, the extended Kondo effect is observed in space beyond the central Mn ion, and onto the nonmagnetic atoms in the molecule.⁹⁶

In addition to dehydrogenation of MPc, the adsorption of hydrogen atoms also changes the spin states of MPc. DFT calculation shows that, after one hydrogen adsorption on the Mn ion of MnPc, the spin polarization decreases in the d_z^2 orbital.⁷⁸ Before the adsorption of hydrogen atoms, there is one spin-up electron in d_z^2 orbital and no spin-down electron. After adsorption, there are one spin-up and one spin-down electrons, respectively. Therefore, the net spin of the Mn ion decreases from $S = 3/2$ to $S = 1$. If there are two more hydrogen atoms adsorbed on MnPc, the most possible configuration is that the two additional hydrogen atoms are attached to two opposite outer nitrogen atoms of the macrocycle. As a result, the net spin is zero.⁷⁸ Besides, small gas molecules adsorbed on the metal center of MPcs also result in a change of molecular conformations. DFT calculation shows that the binding of NO to MPc also leads to the change in electronic states in MnPc, FePc, and CoPc,¹⁰⁸ leading to the HOMO–LUMO gap widens as compared to bare MPc.

Because the Kondo effect relies on the coupling between the localized spin electrons and the conducting electrons, the Kondo effect can be suppressed by a reduced molecular spin state.⁷⁸ Therefore, the spin states and the Kondo resonance of MPc molecules can be manipulated by dosing small molecules such as hydrogen.^{109,110} In Figure 3a it shows a high-resolution STM image of an individual MnPc, and the corresponding atomic configuration and the STM simulation. There is a bright protrusion at the center of the MnPc molecule, which originates from the $3d$ orbital of Mn^{2+} ions. After dosing hydrogen gas at very low temperature, there is a two-dimensional (2D) cluster formed by hydrogen molecule and MnPc.¹¹⁰ A theoretical model is proposed that the interface in-between MnPc and Au(111) serves as a catalyst

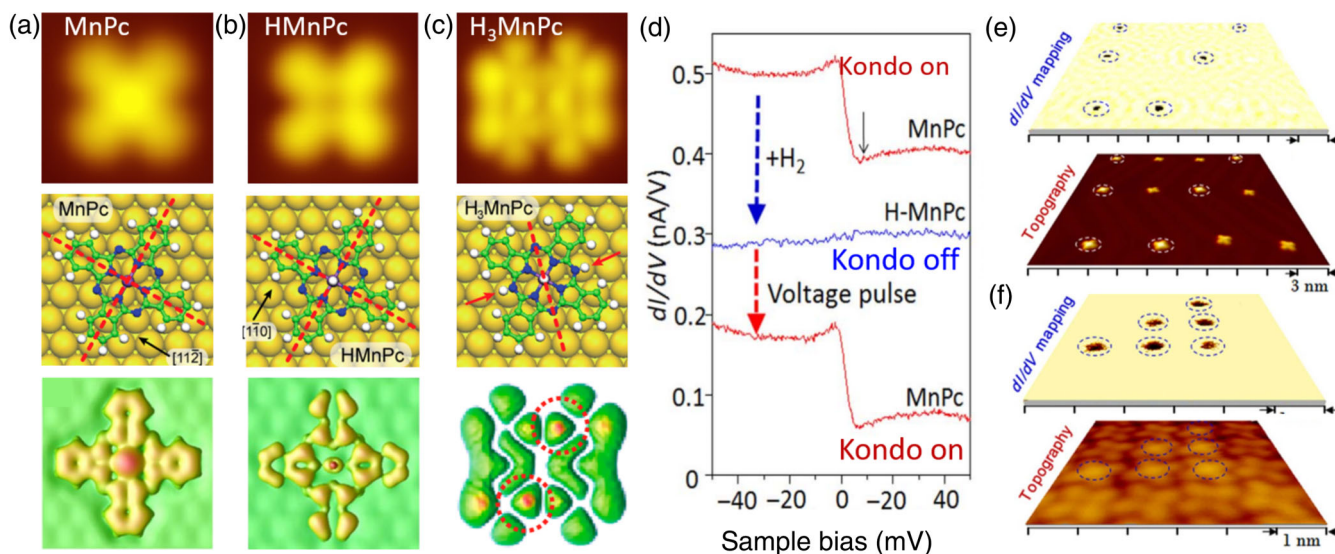


FIGURE 3 Manipulation of MnPc on Au(111) by dosing hydrogen gas. (a–c) STM images, atomic configurations, and STM simulations of MnPc, HMnPc, and H₃MnPc on Au(111), respectively.^{78,109} (d) Sequential variation of the dI/dV measured at the center of a MnPc molecule induced by the absorption and desorption of a single hydrogen atom.⁷⁸ (e, f) The dI/dV mapping (upper panel) and the corresponding topography (lower panel) of (e) a dispersed molecular array and (f) a close-packed molecular array as “a bit with a few selected molecules converted to the MnPc state (Kondo on)”⁷⁸

for hydrogen dissociation at room temperature.¹¹¹ There are atomic hydrogen produced in the MnPc/Au(111) system after dosing hydrogen gas.

After dosing hydrogen gas at room temperature, molecules retained the cross feature but some showed a depression at the center (STM image, atomic configuration, and STM simulation in Figure 3b). A third species (Figure 3c) with D2V symmetry shows a significant change in the molecular orbitals. The topographic features of these three molecules are verified by DFT calculations.^{78,109} The STM simulation has successfully reproduced the main features of STM image of MnPc. In order to get the structure in Figure 3b, several different configurations that contain MnPc and hydrogen were tested. It is found that there is a single hydrogen molecule adsorbed on Mn ion in the center of MnPc, which has the lowest energy. The chemical adsorption of H on MnPc is verified by the calculated binding energy of 1.75 eV. STM simulation shows that there is a depression at the center of MnPc due to the atomic hydrogen adsorption. After one hydrogen atom adsorbed on Mn, there are two hydrogen atoms on two nitrogen atoms of the macrocycle at the opposite sides in MnPc (Figure 3c), which generate a triply hydrogenated MnPc (H₃MnPc). The STM simulation in Figure 3c shows a nice agreement with the STM image. Note that the electron distribution in Figure 3c marked by the red circles show distinctive intensity differences in the left and right part of H₃MnPc, which means the H₃MnPc is a chiral molecule. It indicates that, the symmetry of the system is simply reduced by adding only two more H atoms to HMnPc, without any realignment of the molecular frame.

With a ~ 0.02 ML coverage on Au(111), all MnPc molecules adsorbed at the pointed elbow sites of Au(111).⁸³ After all elbow sites are occupied, additional MnPc molecules separately adsorb on the fcc regions (at coverage of 0.08 ML). At a coverage of 0.15 ML, the MnPc molecules start to adsorb on the hcp regions. After dosing hydrogen gas at room temperature, there is a depression at the molecular center indicating that all MnPc has been changed to HMnPc. HMnPc molecules are anchored at the elbow sites which is similar to the MnPc molecules. However, after the complete occupation of elbow sites, the additional HMnPc molecules adsorb on the hcp regions instead of the fcc regions. Thus, the molecule–substrate interaction for HMnPc molecule on Au(111) is different from that between MnPc and Au(111), which decrease from elbow sites to hcp and fcc regions.⁸³

The attachment of a hydrogen atom changes the d_z^2 orbital of Mn, thus changes the site selectivity of MnPc⁸³ and the magnetic properties.⁷⁸ MnPc molecule has three unpaired electrons so the total spin is $S = 3/2$, which can be detected by a Kondo signal using STM. Figure 3d shows the dI/dV spectra which is measured at the center of MnPc after the absorption and desorption of a single H atom. After the adsorption of a hydrogen atom on the top of Mn ion, the spin polarization decreases in d_z^2 orbital, resulting in the decrease of the total spin from $S = 3/2$ to $S = 1$. Therefore, the Kondo effect is suppressed due to the reduced spin state of Mn ion. The change of molecular morphology from HMnPc to MnPc can be realized by applying voltage pulse. Once the HMnPc state was switched back to the MnPc, the Kondo resonance is fully recovered.

In the experiments, other than the atomic hydrogen, small molecules such as NO, CO, and O₂, are also observed to adsorb at the center metal ion of MPC. The adsorption of NO on CuPc on highly oriented pyrolytic graphite (HOPG) resulting in p-doped graphene due to the electron transfer from HOPG to NO/CuPc.¹¹² The experiment verified that the existence of Kondo resonance can be controlled by the adsorption or desorption of CO molecule in the MnPc/Bi(110) system.¹¹³ Oxygen gas can be dissociated in the system of FePc/Ag(111), leaving the structure where the FePc molecule locates on top site of Ag(111), and interacts with two oxygen atoms adsorbed at “the neighboring short-bridge sites.”¹¹⁴ Therefore, it is an efficient method to control the spin states of MPC by dosing small molecules.

2.4 | High-density data storage based on MPC/Au(111) system

Organic semiconductors, which are based on the electron pull–push effect, have become alternatives to traditional inorganic semiconductors in memory-devices.^{115,116} The devices exhibit stable ON/OFF electronic states, which have been realized by polymer,^{117–119} dimeric hydrazine,¹²⁰ aminobenzene sulfonated compound,¹²⁰ and so forth. Different from the electron pull–push effect, a design of high-density data storage device based on ON/OFF spin states has been proposed. The appearance or disappearance of the Kondo resonance at a single atom site can be used as a single bit of information and suggests applications in information recording and storage at the ultimate molecular limit when combined with STM manipulations.

DFT calculations show that the adsorption of hydrogen will change the Kondo resonance of Mn ion from on state to off state in MnPc on Au(111), which can be used as a bit of information. Therefore, researchers devoted to grow MnPc arrays to realize high-density storage. At the initial state, all the MnPc molecules are converted to the HMnPc

molecules by dosing hydrogen. Figure 3e shows the topography and dI/dV mapping in a MnPc molecular array after applying voltage pulses on the selected HMnPc (marked by dashed circles). Therefore, the HMnPc molecules in the array are back to MnPc molecules, and the dI/dV mapping shows dark dots due to the Kondo resonance of the MnPc. In the constructed MnPc monolayer similar to the previous Figure 1d,f, this process can be also realized (Figure 3f). By attaching or detaching a single hydrogen atom, the on/off Kondo effect can be reversibly controlled at the molecule level. The molecular Kondo system can be used in “nonvolatile data recording and storage at the ultimate molecule limit.”⁷⁸

3 | MOLECULAR SELF-ASSEMBLY ENHANCED SELECTIVITY AND ACTIVITY OF ON-SURFACE REACTIONS

On-surface synthesis is a popular method for fabricating low-dimensional supermolecular networks^{30,121,122} because of the catalytic activity of metal surface.^{123,124} One of the biggest challenges in on-surface synthesis is controlling site selectivity, which is to differentiate the reactivity among the same kind of functional groups.^{125,126} The specificity of chemical reaction pathway is realized by the symmetry-broken of reactants. One of the strategies is to introduce steric hindrance via non-covalent interactions.^{127,128} Moreover, the local non-covalent intermolecular interactions between reactants on metal surfaces also provide opportunities to tailor the reaction pathway. The well-ordered assembled structure of reactants serves as a template, and contributes to high selectivity of one single product among several isomers.^{129,130}

First-principles calculation is a powerful tool to investigate the chemical reaction from the perspective of both kinetics and thermodynamics. The yield of one product in selective reaction can be predicted by the activation energy, which is the energy difference between the initial state and transition state. The transition-state energy can be calculated using nudged elastic band,¹³¹ which is a method for finding saddle point and minimum energy path. The accurate calculations should reproduce the main features of experimental results of molecules on metal surfaces, including adsorption sites, binding energies, and diffusion barriers. Therefore, the vdW functionals are of great importance in on-surface reactions. For example, in the case of selective dehydrogenation of formic acid (HCOOH) on Pt(111) surface,¹³² the improved vdW corrected methods^{50,133,134} and optimized vdW functionals^{52,135} perform well to estimate the adsorption energies. However, the optimized vdW functionals overestimate barrier difference between C–H and O–H bond breaking, and fail to describe the catalytic selectivity. Therefore, to correctly predict the catalytic activity and selectivity of different reaction pathways,¹³⁶ the vdW functionals need to give the same accuracy towards all key adsorbates in on-surface reaction. Besides, ab initio molecular dynamics simulations, which consider steric and temperature effects, enable understanding the bond dissociation and reforming process during chemical reaction. Those methods provide theoretical insights for the investigations of reaction mechanism on self-assembly in selective reactions.

3.1 | Selectivity in intermolecular reaction

The main challenge for increasing the reaction selectivity through self-assembly strategy is the stability of the well-ordered assemblies during the reaction process. While annealing to high temperature, the self-assembled structure connected by weak van der Waals interactions or hydrogen bonds, is easily to be destroyed. By replacing the hydrogen with fluorine in some of the benzene rings in the organic precursors, the stability of self-assembly of reactants is enhanced,¹³⁷ because the fluorine acts as a hydrogen-bond acceptor in many systems and improves the strength of intermolecular interaction.¹³⁸

Figure 4a,b shows the disordered and ordered structures of 4,4'-bis(2,6-difluoropyridin-4-yl)-1,1':4',1''-terphenyl (BDFFTP) on Au(111).¹³⁹ Two potential reaction pathways are proposed in Figure 4e, including dehydrocyclization (DHC) (pathway 1) and coupling reaction (pathway 2). The calculated energy changes for both coupling and DHC products without considering self-assembly show that, both the pathway 1 and 2 are endothermic, indicating that they have to take place at elevated temperatures. The energy needed for the coupling reaction is much higher than that for the DHC reaction, suggesting that the coupling reaction is less favorable than the DHC one. However, in the self-assembled close-packed structures, the repulsion interaction between neighboring C–F bonds make the ends of each rotating BDFFTP molecule closed to positions D2 or D3 of the un-rotated BDFFTP molecules. Because of steric hindrance, the coupling reaction and DHC reaction at D1 and D4 are difficult.

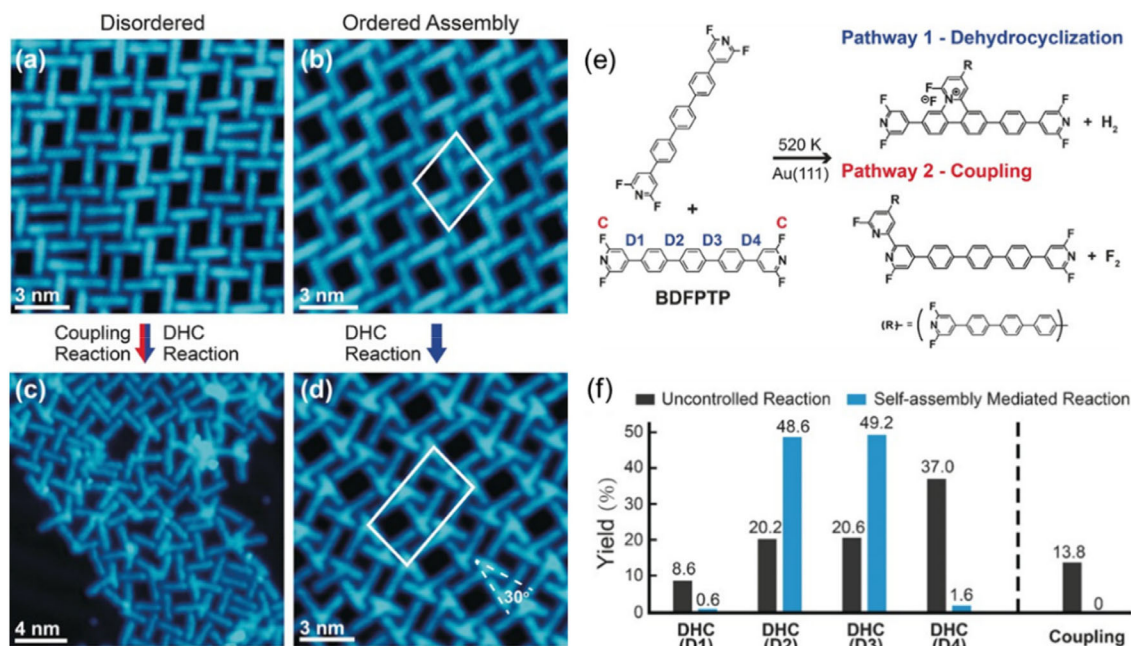


FIGURE 4 Selectivity of dehydrocyclization and coupling reaction pathways of BDFPTP on Au(111).¹³⁹ (a,b) STM images of ordered and disordered assembly structures of BDFPTP. (c,d) Products from (a) and (b) after annealing at 520 K. (e) Dehydrocyclization and coupling reaction pathways of BDFPTP on Au(111). D1–D4 are the reaction sites for dehydrocyclization and C is the potential reaction site for coupling. (f) Statistic histograms of the products from disordered (black bars) and ordered (blue bars) structures

The experimental results agree with the theory predictions. By controlling the annealing rate, the authors can fabricate both ordered and disordered self-assemblies of BDFPTP on Au(111) (Figure 4c,d). A distinct distribution of products is formed after the thermal treatment at 520 K of the two samples. The main products in the ordered self-assembly regions are the products from DHC at D2 and D3 sites (Figure 4f).¹³⁹ The yield of the main product is about 98%, while there is no product generated from coupling reaction. In contrast in the disordered region, the products are distributed randomly. The amounts of products which are from the four DHC reactions occurring in D1–D4 sites and the ones which are generated from coupling reactions, are almost equal. The absence of product selectivity is the result of “the random distribution of BDFPTP in the disordered self-assemblies.”¹³⁹ It indicates that the molecular self-assembly can efficiently steer on-surface reaction pathways.

3.2 | Selectivity in intramolecular reaction

The fluorine substitution strategy can be used in intramolecular reactions to enhance the selectivity of one specific product. Tetraphenylporphyrins (TPPs) and tetrakis(pentafluorophenyl)porphyrins (TPFPs) undergo a quadruplicate intramolecular cyclization on the metal surface upon thermal treatment. There are two mechanisms which can describe the reaction pathways. One is that the reaction follows the principle of equal probability. Due to the possibility of cyclodehydrogenation at either side of the benzene ring, there are four planar isomers, as shown in Figure 5a. The expected frequencies of four products (I, II, III, and IV) based solely on probability should be 1/2, 1/4, 1/8, and 1/8, respectively. The other is the reaction follows the Boltzmann distribution, in which the ratio of probabilities of the products only depends on the energy differences. DFT calculations were performed on all products to illustrate the origin of selectivity in different systems. For 2H-TPP, product I is the ground state, and the energy of products II, III, and IV is 0.18, 0.42, and 0.26 eV higher than that of I, respectively.¹⁴⁰ For Fe-TPFP, product IV has the lowest energy, and the energy of products I, II, and III is 0.56, 0.26, and 0.24 eV higher than IV, respectively.¹⁴¹ Therefore, if the reaction depends completely on the energy differences, there are only products I in 2H-TPP and products IV in Fe-TPFP, respectively. Besides, the final products of other metal-TPPs such as Co-TPP and Ru-TPP are more likely to be IV, because the structure and symmetry of metal-TPPs are similar to Fe-TPFP.

However, the experimental results are not in agreements with the simple predictions based on these two mechanisms, indicating there are other important factors that affect the chemical reaction. Figure 5b–d are the STM images of

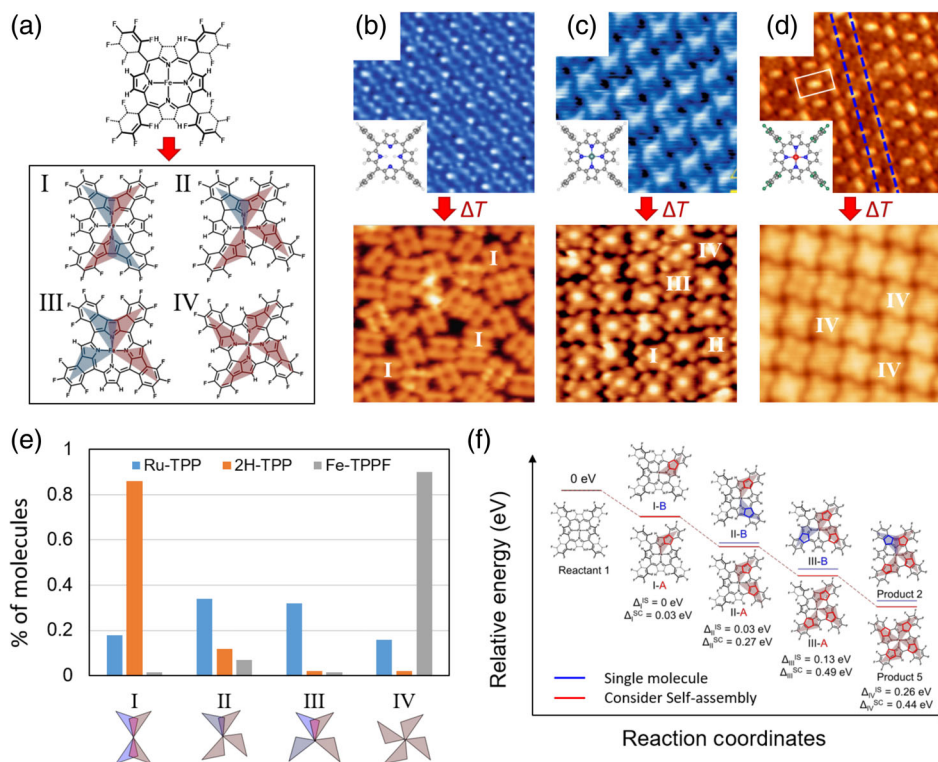


FIGURE 5 Selectivity of on-surface cyclization of different tetraphenylporphyrins (TPPs). (a) A schematic showing four isomers after on-surface intramolecular quadruple ring formation. (b) STM images of 2H-TPP molecules and the products after annealing the surface to 620 K.¹⁴⁰ (c) STM images of Ru-TPP molecules and the products after annealing the surface to 560 K.¹⁴⁰ (d) STM images of Fe-TPFP molecules and the products after annealing the surface to 600 K.¹⁴¹ (e) Histogram of different planar porphyrin derivatives of Ru-TPP (blue), 2H-TPP (orange), and Fe-TPFP (gray). In the histogram, the original data are re-plotted. (f) Comparison of energies of intermediates along different reaction pathways for free-standing Fe-TPFP and Fe-TPFP/Au(111). Δ_I^{IS} , Δ_{II}^{IS} , Δ_{III}^{IS} , and Δ_{IV}^{IS} are energy differences between the lowest and second lowest structures when there is an isolated intermediate, while Δ_I^{SC} , Δ_{II}^{SC} , Δ_{III}^{SC} , and Δ_{IV}^{SC} are the energy differences considering steric constraints coming from the neighboring molecules¹⁴¹

three different TPPs: 2H-tetraphenylporphyrin (2H-TPP), Ru-tetraphenylporphyrin (Ru-TPP),¹⁴⁰ and iron(II)-tetrakis(pentafluorophenyl)-porphyrin (Fe-TPFP),¹⁴¹ and their products after annealing. The upper panels show the self-assembly of those TPP molecules before reaction, and the bottom panels show the products. After adsorbed on metal surface, TPP molecules exhibit a saddle-shaped conformation and form a dense-packed layer stabilized by T-type interactions between the terminal phenyl groups molecule which is a characteristic feature of metal porphyrins adsorbed on metal surfaces.^{142–144} Because of the saddle-shaped conformation, the iron atom in TPP molecule undergoes high spin-polarized states with a magnetic moment of 4 μ_B .¹⁴³ However, due to the substitution of hydrogen with fluorine in the benzene rings, the self-assembly of Fe-TPFP, which has a rectangular unit cell containing two molecules with different azimuthal orientation, is slightly different with 2H-TPP and Ru-TPP.

After annealing to ~ 600 K, the yield of the four reaction products is very different. Figure 5e is the histogram of different products generated from Ru-TPP (red), 2H-TPP (yellow), and Fe-TPFP (green). For 2H-TPP, 86% of the products is product I. Only 12% of the products are II. Less than 3% of the products are III or IV. For Ru-TPP, products II and III amount to slightly more than 30%, and I and IV to less than 20%. For Fe-TPFP, the overwhelming majority (more than 90%) of products is IV, in which the products are self-assembling into a new 2D structure on the Au(111) surface. Other products are only observed in the amorphous region at boundaries.

In order to describe the evolution pathway, a series of possible intermediates are investigated by calculating their ground state energies on Au(111). Because the reactions in each step (dehydrogenation/dehydrofluorization and C—C bond formation) are very similar, the activation energy in the reaction is correlated to the adsorption energies of intermediates, according to the universality principle Brønsted–Evans–Polanyi relation.¹⁴⁵ First, the authors calculate the total energies of all possible single intermediates. All intermediates in the reaction pathway from Fe-TPFP to IV is the most energy-favorable path. However, the energy difference between intermediates which has the lowest and second-

lowest energy in step 2 is only 0.03 eV, as shown in Figure 7f, indicating that other products are also very likely to be formed at an annealing temperature of 600 K. These results are in contrast to the fact that there are no other products observed in the self-assembled region of product IV.

Furthermore, similar to the case of isolated molecules, the ground state energies of all intermediates considering steric constraints are calculated. The two product species II and IV as well as their intermediates are relaxed in a self-assembled structure. The energy differences of the main species are in Figure 5f. No significant difference shows in the first step, while the following steps favor the path to the final product. The difference between the product II and the final product IV is 0.44 eV. Therefore, the self-assembly of reactants can significantly enhance the stereoselectivity.

This concept is verified by experiments with varying coverage and heating rate. At lower coverages (~ 0.1 ML), the stereoselectivity towards product IV is less pronounced ($\sim 20\%$). At lower heating rates, the selectivity of the product IV decreases significantly, even though the coverage is very high. The ratio of product IV increases from 30% to 90% when the heating rate increases from 1 to 15 K/min. It indicates that the “robustness” of self-assembly during reaction has a significant influence on the stereoselectivity.

3.3 | Enhanced catalytic activity at molecule–metal interface

Furthermore, the catalytic activity can be enhanced at the molecule–metal interface. A “quantum nutcracker” for H_2 dissociation is theoretically predicted to be active at near-room temperature.¹¹¹ The quantum nutcracker consists of two jaws: MPc and the metallic surface (e.g., Au(111) and Cu(111) surfaces, and can be realized on other metallic surfaces¹⁴⁶). The two components are weakly bonded by van der Waals interaction. In the case of MPc and Au(111), both MPc molecules and Au(111) surface are inert for hydrogen dissociation, although the H_2 dissociation on Au(111) was investigated for fundamental science purposes^{147–149} and gold nano-clusters show activity due to quantum-size effect.¹⁵⁰ At the beginning of the dissociation process, H_2 diffuses on the Au(111) and then goes into the channel between the MPc and Au(111). After that, H_2 bond splits via a cooperative quantum interaction with the two jaws. Finally, the atomic H leaves the channel. The researchers find that the overall activation barrier for both Au- and Cu-based quantum nutcrackers can be overcome near room temperature. Unlike the usual searches for catalysts that mainly focus on thermodynamics and kinetics, the discovery of the quantum nutcracker, based on inexpensive materials that by themselves are inert, expands the prospects of creating catalytic systems by exploiting structural and electronic properties. Experiments of dosing hydrogen gas to MnPc/Au(111) system found that all MnPc molecules become HMnPc,⁷⁸ demonstrating the activity of MnPc/Au system for hydrogen dissociation. Temperature dependent experiments show that the MnPc/Au system is active at temperatures higher than 120 K.

4 | 2D METAL–ORGANIC NETWORKS WITH NOVEL PROPERTIES

Self-assembly of organic molecules can form 2D metal–organic networks with appropriate metals. The 2D metal–organic networks have attracted attention because the interaction between organic ligands and metal atoms is much stronger than between organic molecules due to the coordination bonds. The strong interaction gives rise to strong electron overlap between neighboring units. The organic ligands used to constructing 2D metal–organic networks are usually π -conjugated systems. The π -d conjugated system possesses exotic electronic properties,^{151–154} which relies on the constructed structures. For example, the 2D organic network consisting of three Cu atoms and one benzenehexathiol molecule ($Cu_3(C_6S_6)$) has high electrical conductivity¹⁵⁵ and superconductivity,^{156,157} while the one consisting of three Ni atoms and two benzenehexathiol molecules ($Ni_3(C_6S_6)_2$) has topological non-trivial band structure.^{158,159} In this part, we start from the 2D metal–organic systems with topological insulator states, then we introduce the 2D metal–organic network with superconductivity.

The first-principles calculations can be transformed into a unique set of maximum localized Wannier functions (WFs).¹⁶⁰ This connection enables the use of WFs in the construction of model Hamiltonians, and allows for an exact description of bands in a certain energy range, helping us understanding the physical nature of the novel topological materials.¹⁶¹

4.1 | 2D metal–organic topological insulator

So far, there are two types of 2D topological insulators predicted. One has a hexagonal lattice,¹⁶² in which metal atoms form a hexagonal structure and bond to three adjacent molecules, as shown in Figure 6a.¹⁶³ The hexagonal lattice is composed of benzene rings and metal atoms with threefold rotational symmetry, in which the metal–C bonds are sp^3 hybridized. The optimized 2D lattice shows the metal atoms are up and down out of the plane of benzene rings¹⁶³ (side view in Figure 6a). If the metal atom is Pb, the equilibrium lattice constant is 12.36 Å, with the Pb–Pb distance of 7.46 Å and height of 2.18 Å, respectively. The electronic band structure in Figure 6d shows a Dirac cone at the K point. The Fermi level is exactly at the Dirac point without spin–orbit coupling (SOC), while there is a gap of ~ 8.6 meV at the K point with SOC, indicating the nature of intrinsic topological insulator states. The topological edge states are calculated by a tight-binding Hamiltonian in the basis of the maximally localized WFs, which can be fitted to the first-principles band structure.

The other type has a Kagome lattice,^{159,164–167} in which three metal atoms form a Kagome lattice and bond the adjacent two organic molecules, as shown in Figure 6b ($\text{Ni}_3(\text{C}_6\text{S}_6)_2$).¹⁵⁸ Figure 6e shows the band structure of $\text{Ni}_3(\text{C}_6\text{S}_6)_2$ with SOC around the Fermi level. There are typical Kagome bands consisting of one flat band above two Dirac bands. The band gap of the Dirac band (Δ_1) is 13.6 meV, while the band gap between the flat band and the top Dirac band (Δ_2) is 5.8 meV. Moreover, there exists spontaneous magnetization in a 2D topological insulator. The quantum anomalous Hall effects (QAHE) can be realized in 2D topological insulators based on metal–organic networks.¹⁶⁸ The Cucyanobenzene (DCB) lattice is a stable QAHE insulator with a ferromagnetic ground state (Figure 6c). The typical Kagome bands around the Fermi level are only occupied by single-spin electrons, as shown in Figure 6f. After considering SOC, there is a band gap ($\Delta_1 = 2.0$ meV) between the flat band and the top Dirac band, while the Fermi level is in the SOC gap.

Theoretical prediction shows that the 2D Cu-9,10-dicyanoanthracene (DCA) lattice is a topological insulator.¹⁶⁹ The 2D Cu–DCA hexagonal network is constructed by two Cu atoms and three DCA molecules, including a hexagonal lattice contributed by Cu atoms and a Kagome lattice contributed by DCA molecules, as shown in Figure 7a. Because of

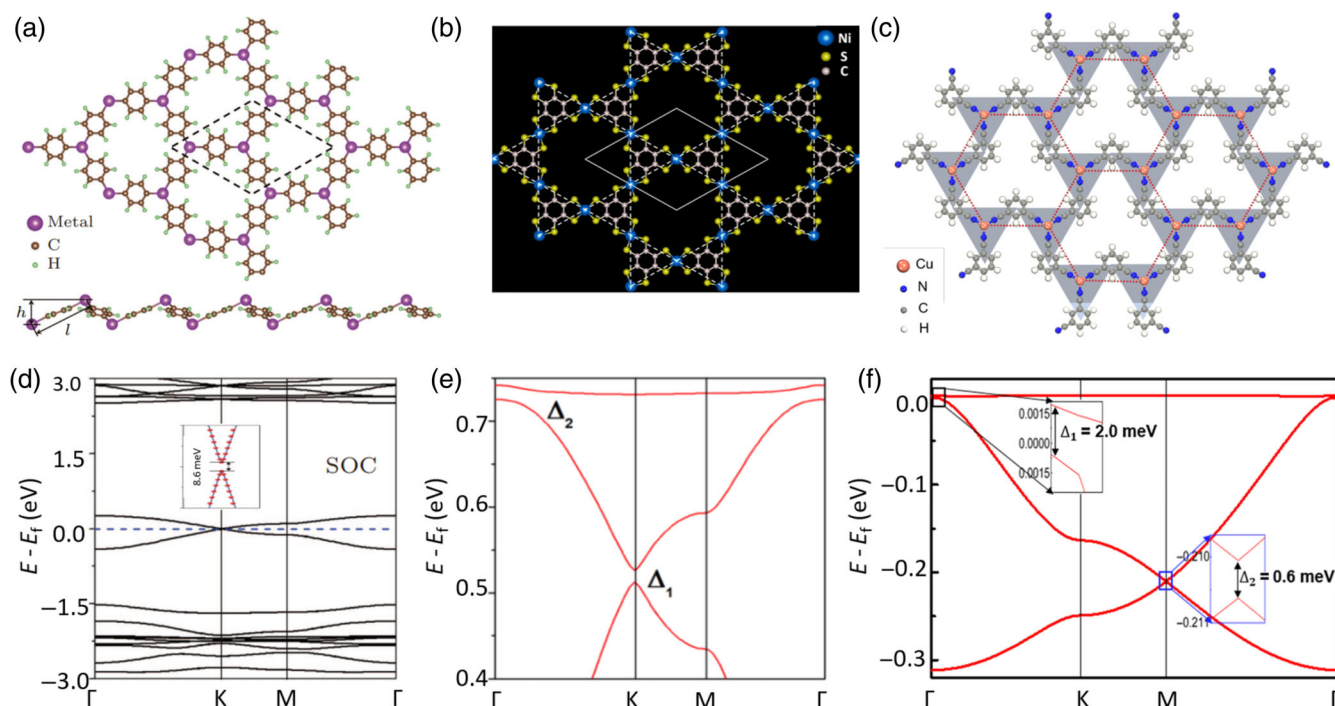


FIGURE 6 Theoretical predicted organic topological insulators. (a) Atomic structure and electronic properties of monolayer $\text{Pb}(\text{C}_6\text{H}_5)_3$ in a hexagonal metal–organic lattice.¹⁶³ (b) Atomic structure of monolayer $\text{Ni}_3\text{C}_{12}\text{S}_{12}$ in a Kagome metal–organic lattice.¹⁵⁸ (c) Atomic structure of Cu-DCB CT lattice which has a ferromagnetic ground state.¹⁶⁸ (d), (e) and (f) are the band structures of (a), (b) and (c) near the Fermi level with SOC, respectively

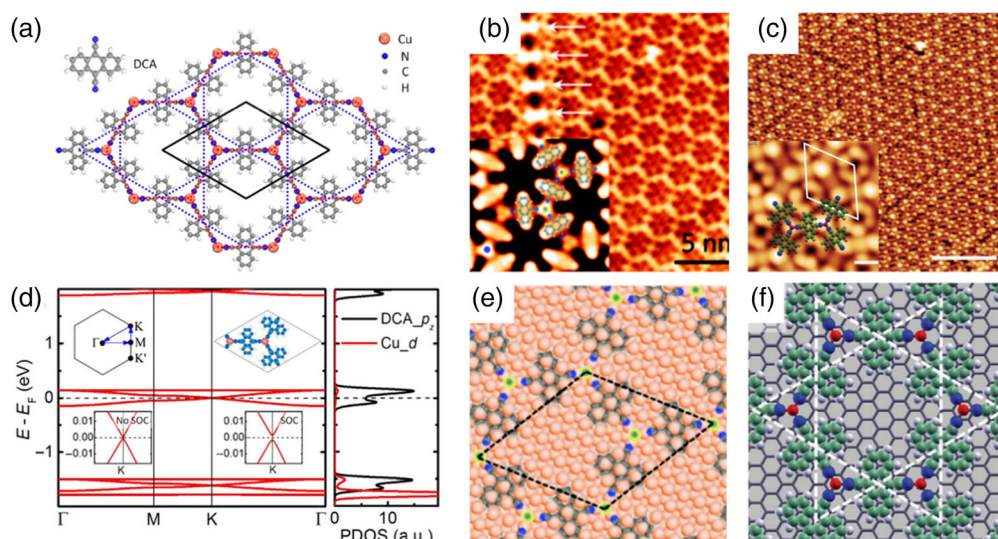


FIGURE 7 Metal-organic topological insulator Cu-DCA. (a) Atomic structure of Cu-DCA.¹⁶⁹ (d) The band structure and PDOS of Cu-DCA, where the top-right inset is the charge distribution around the Fermi level, and the bottom two insets are the zoom-in bands without and with SOC, respectively.¹⁶⁹ (b,c) STM images of Cu-DCA grown on Cu(111)¹⁷⁰ and graphene,¹⁷¹ respectively. The corresponding configurations are shown in (e) and (f)

the lone pair in the CN group in the 9,10-DCA molecule, the molecule forms strong coordination bonds with the Cu atoms.

This Cu-DCA lattice has already been synthesized in the experiment.^{170,171} A regular, porous 2D network is formed after desorption DCA molecules onto Cu(111) surface at room temperature, as shown in Figure 7b.¹⁷⁰ As shown in Figure 7e, the Cu atoms form a honeycomb lattice, and the DCA molecules form a Kagome lattice. Moreover, the Cu-DCA lattice is also fabricated on graphene, as shown in Figure 7c. After depositing DCA molecules and Cu atoms sequentially onto the graphene (Gr/Ir(111)) substrate at room temperature, a 2D Cu-DCA hexagonal network formed. The atomic structure is shown in Figure 7f.¹⁷¹ The band structures and PDOS of Cu-DCA lattice are shown in Figure 7d. It shows a typical Kagome band around the Fermi level, including one flat band and two Dirac bands. A band gap lies at the Dirac point after the SOC is included, indicating the very nature of intrinsic topological insulator states with SOC.

4.2 | 2D metal-organic superconductor

Besides, the superconductivity in 2D metal-organic network has been predicted¹⁵⁶ and also been verified experimentally.¹⁵⁷ Cu-benzenehexathial ($\text{Cu}_3(\text{C}_6\text{S}_6)$, Cu-BHT), a Kagome lattice with the point group of D_{6h} , is consist of copper atoms and C_6S_6 (BHT) molecules (Figure 8a).¹⁵⁶ There are bands across the Fermi level, as shown in the band structures in Figure 8b. In Figure 8d, the Fermi surface of Cu-BHT in the upper panel shows that there are several hole/electron pockets in the Brillouin zone. The bottom panel shows the momentum-dependent coupling λ_q . It indicates that the σ -band-like electron/hole pockets at the boundary of BZ contributes to the electron-phonon coupling (EPC). On the other hand, the π -band-like hole pockets at Γ point make small contributions to EPC. Figure 8e shows the Eliashberg spectral function $\alpha^2F(\omega)$ with the cumulative frequency-dependent EPC strength $\lambda(\omega)$, and the projected phonon density of state (PhDOS) of different atoms (middle panel and lower panel). The results indicate that the main contribution is from the out-of-plane vibrations of S atoms, due to a peak in $\alpha^2F(\omega)$ at the frequency around 50 cm^{-1} . Besides, the out-of-plane vibrations of Cu atoms also contribute to the small increase of EPC at the frequency around 100 cm^{-1} . The logarithmically averaged frequency is calculated to be 51.8 K (35.96 cm^{-1}).¹⁵⁶ The Curie temperature is 4.43 K .¹⁵⁶ The authors also found that bulk Cu-BHT is also a SC with T_c of 1.58 K .¹⁵⁶

The experiment has verified the superconductivity in Cu-BHT.¹⁵⁷ Cu-BHT films are fabricated at the liquid-liquid interface and then then transferred on the substrate. Figure 8c shows the high-resolution STEM image of Cu-BHT.¹⁵⁷

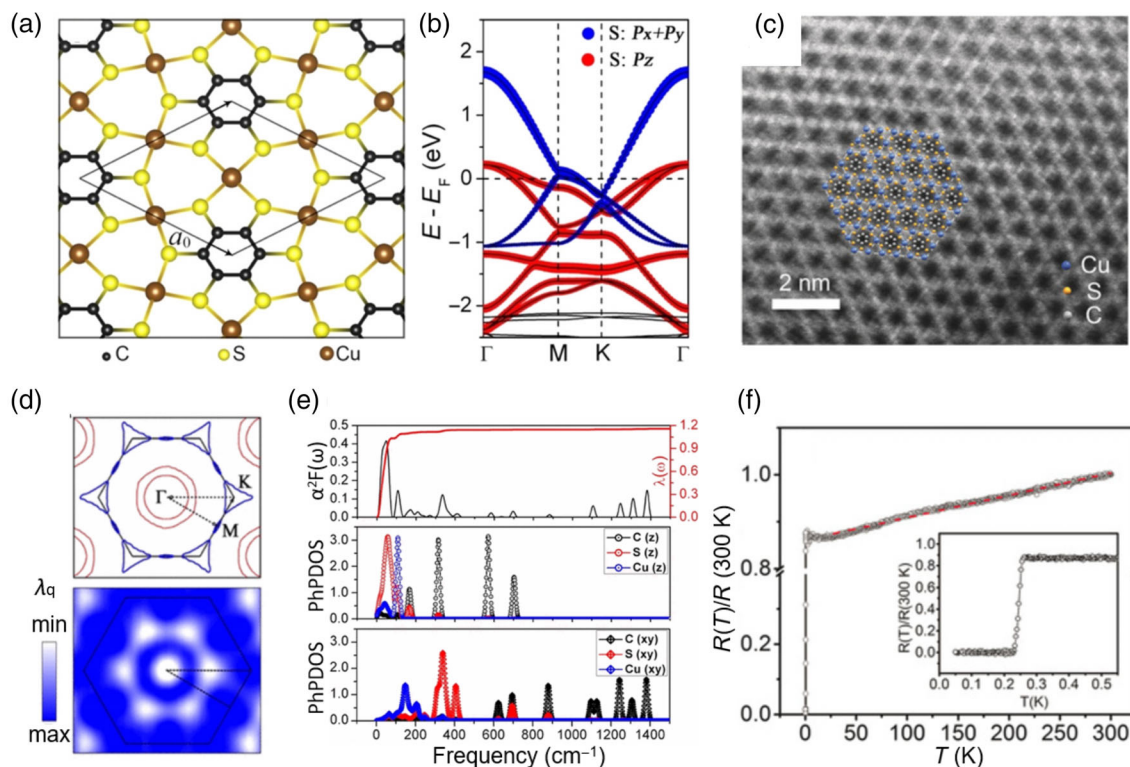


FIGURE 8 Superconductivity in Cu-BHT. (a) The structure of Cu-BHT.¹⁵⁶ (b) Band structure contributed by the p_z and $p_x + p_y$ orbitals of S atoms marked by red and blue, respectively.¹⁵⁶ (c) High-resolution STEM image of Cu-BHT.¹⁵⁷ (d) The Fermi surface contour in the reciprocal space and the distribution of q -resolved electron–phonon coupling λ_q . (e) Eliashberg spectral function $\alpha^2 F(\omega)$ and projected phonon density of state (PhDOS) of single layer Cu-BHT.¹⁵⁶ (f) Temperature dependence of the normalized resistance $R(T)/R(300)$ from 50 mK to 300 K. Inset: expanded scale for temperatures near the superconducting transition¹⁵⁷

Figure 8f shows the temperature dependence of electrical resistance measured on Cu-BHT.¹⁵⁷ The Curie temperature for superconducting transition is 255 mK.

5 | CONCLUSION

Self-assembly of organic molecules on metal surfaces is a simple and efficient way to fabricate low-dimensional supramolecular materials. The cooperation of theoretical calculations and experiments accelerates the process of investigation of self-assembly and the further exploration of potential applications. In this review, we introduce the novel properties and potential applications in high-density data storage, selective reaction, and quantum topological device. The investigation of the physical and chemical properties of self-assembled structures and the mechanism that controls the self-assembly behavior can not only provide guidance for the construction and manipulation of functional materials based on low-dimensional supramolecular network, but also provide theoretical foundations for the further applications. The researches of molecular self-assemblies depend much on the developments of computational methods. To achieve calculations with high accuracy, the exchange-correlation functionals and van der Waals corrections need to be improved with better descriptions on metal–organic interactions. In recent years, there are many efforts on database-driven high-throughput calculation^{172,173} and machine learning,¹⁷⁴ which are the promising computational techniques in material sciences.¹⁷⁵ The development of the computational technology will contribute to the design of molecular self-assembly with novel properties and their further applications.

ACKNOWLEDGMENTS

The authors would like to thank Yixuan Gao, Jinbo Pan, and Hui Chen for discussions.

CONFLICT OF INTEREST

The authors have declared no conflicts of interest for this article.

DATA AVAILABILITY STATEMENT

Data sharing is not applicable to this article as no new data were created or analyzed in this study.

AUTHOR CONTRIBUTIONS

Lei Tao: Formal analysis (equal); writing – original draft (equal); writing – review and editing (equal). **Yu-yang Zhang:** Funding acquisition (equal); writing – review and editing (equal). **Shixuan Du:** Funding acquisition (equal); resources (equal); supervision (equal); writing – review and editing (equal).

ORCID

Yu-yang Zhang  <https://orcid.org/0000-0002-9548-0021>

Shixuan Du  <https://orcid.org/0000-0001-9323-1307>

RELATED WIREs ARTICLE

[One molecule, two states: Single molecular switch on metallic electrodes](#)

REFERENCES

1. Böhringer M, Morgenstern K, Schneider WD, Berndt R, Mauri F, de Vita A, et al. Two-dimensional self-assembly of supramolecular clusters and chains. *Phys Rev Lett.* 1999;83(2):324–7.
2. Pawin G, Wong KL, Kwon KY, Bartels L. A homomolecular porous network at a Cu(111) surface. *Science.* 2006;313(5789):961–2.
3. Dong S, Zhang H, Yang L, Bai M, Yao Y, Chen H, et al. Solution-crystallized organic semiconductors with high carrier mobility and air stability. *Adv Mater.* 2012;24(41):5576–80.
4. Ghosh S, Philips DS, Saeki A, Ajayaghosh A. Nanosheets of an organic molecular assembly from aqueous medium exhibit high solid-state emission and anisotropic charge-carrier mobility. *Adv Mater.* 2017;29(10):1605408.
5. Chen H, Cheng N, Ma W, Li M, Hu S, Gu L, et al. Design of a photoactive hybrid bilayer dielectric for flexible nonvolatile organic memory transistors. *ACS Nano.* 2016;10(1):436–45.
6. Liu S, Wei Z, Cao Y, Gan L, Wang Z, Xu W, et al. Ultrasensitive water-processed monolayer photodetectors. *Chem Sci.* 2011;2(4):796–802.
7. Adonin SA, Udalova LI, Abramov PA, Novikov AS, Yushina IV, Korolkov IV, et al. A novel family of polyiodo-bromoantimonate(III) complexes: cation-driven self-assembly of photoconductive metal-polyhalide frameworks. *Chem Eur J.* 2018;24(55):14707–11.
8. Gambardella P, Stepanow S, Dmitriev A, Honolka J, de Groot FMF, Lingenfelder M, et al. Supramolecular control of the magnetic anisotropy in two-dimensional high-spin Fe arrays at a metal interface. *Nat Mater.* 2009;8(3):189–93.
9. Guo M, Jiang J, Qian J, Liu C, Ma J, Nan CW, et al. Flexible robust and high-density FeRAM from array of organic ferroelectric nanolamellae by self-assembly. *Adv Sci.* 2019;6(6):1801931.
10. Hu Z, Tian M, Nysten B, Jonas AM. Regular arrays of highly ordered ferroelectric polymer nanostructures for non-volatile low-voltage memories. *Nat Mater.* 2009;8(1):62–7.
11. Gorbunov AV, Garcia Iglesias M, Guilleme J, Cornelissen TD, Roelofs WSC, Torres T, et al. Ferroelectric self-assembled molecular materials showing both rectifying and switchable conductivity. *Sci Adv.* 2017;3(9):e1701017.
12. Viswanath P, de Silva KKH, Huang HH, Yoshimura M. Large piezoresponse in ultrathin organic ferroelectric nano lamellae through self-assembly processing. *Appl Surf Sci.* 2020;532:147188.
13. Bera S, Guerin S, Yuan H, O'Donnell J, Reynolds NP, Maraba O, et al. Molecular engineering of piezoelectricity in collagen-mimicking peptide assemblies. *Nat Commun.* 2021;12(1):2634.
14. Li P, Jia C, Guo X. Molecule-based transistors: from macroscale to single molecule. *Chem Rec.* 2021;21(6):1284–99.
15. Hu Z, Lin Z, Su J, Zhang J, Hao Y, Chang J, et al. Controllable self-assembly of PTCDI-C8 for high mobility low-dimensional organic field-effect transistors. *ACS Appl Electron Mater.* 2019;1(10):2030–6.
16. Schön JH, Meng H, Bao Z. Self-assembled monolayer organic field-effect transistors. *Nature.* 2001;413(6857):713–6.
17. Kubo Y, Maeda S, Tokita S, Kubo M. Colorimetric chiral recognition by a molecular sensor. *Nature.* 1996;382:522–4.
18. James TD, Samankumara Sandanayake KRA, Shinkai S. Chiral discrimination of monosaccharides using a fluorescent molecular sensor. *Nature.* 1995;374:345.
19. Rojas MT, Kaifer AE. Molecular recognition at the electrode-solution interface. Design, self-assembly, and interfacial binding properties of a molecular sensor. *J Am Chem Soc.* 1995;117(21):5883–4.
20. Vijayakumar C, Tobin G, Schmitt W, Kim MJ, Takeuchi M. Detection of explosive vapors with a charge transfer molecule: self-assembly assisted morphology tuning and enhancement in sensing efficiency. *Chem Commun.* 2010;46(6):874–6.
21. Della Rocca J, Liu D, Lin W. Nanoscale metal-organic frameworks for biomedical imaging and drug delivery. *Acc Chem Res.* 2011;44(10):957–68.

22. Zheng Y, Sun FZ, Han X, Xu J, Bu XH. Recent progress in 2D metal-organic frameworks for optical applications. *Adv Opt Mater.* 2020; 8(13):2000110.
23. Wang Z, Jingjing Q, Wang X, Zhang Z, Chen Y, Huang X, et al. Two-dimensional light-emitting materials: preparation, properties and applications. *Chem Soc Rev.* 2018;47(16):6128–74.
24. Chen Y, Wang C. Designing high performance organic batteries. *Acc Chem Res.* 2020;53(11):2636–47.
25. Zhao S, Wang Y, Dong J, He CT, Yin H, An P, et al. Ultrathin metal-organic framework nanosheets for electrocatalytic oxygen evolution. *Nat Energy.* 2016;1(12):16184.
26. Dhakshinamoorthy A, Asiri AM, Garcia H. 2D metal-organic frameworks as multifunctional materials in heterogeneous catalysis and electro/photocatalysis. *Adv Mater.* 2019;31(41):1900617.
27. Harikumar KR, Lim T, McNab IR, Polanyi JC, Zotti L, Ayissi S, et al. Dipole-directed assembly of lines of 1,5-dichloropentane on silicon substrates by displacement of surface charge. *Nat Nanotechnol.* 2008;3:222–8.
28. Stepanow S, Lingensfelder M, Dmitriev A, Spillmann H, Delvigne E, Lin N, et al. Steering molecular organization and host-guest interactions using two-dimensional nanoporous coordination systems. *Nat Mater.* 2004;3:229–33.
29. Theobald JA, Oxtoby NS, Phillips MA, Champness NR, Beton PH. Controlling molecular deposition and layer structure with supramolecular surface assemblies. *Nature.* 2003;424:1029–31.
30. Lu J, Bao DL, Dong H, Qian K, Zhang S, Liu J, et al. Construction of two-dimensional chiral networks through atomic bromine on surfaces. *J Phys Chem Lett.* 2017;8(2):326–31.
31. Xiao W, Ruffieux P, Ait-Mansour K, Gröning O, Palotas K, Hofer WA, et al. Formation of a regular fullerene nanochain lattice. *J Phys Chem B.* 2006;110(43):21394–8.
32. Huheey JE, Keiter EA, Keiter RL. *Inorganic Chemistry: Principles of Structure and Reactivity.* 4th ed. Hoboken, NJ: Prentice Hall PTR; 1993.
33. Giancarlo LC, Flynn GW. Raising flags: applications of chemical marker groups to study self-assembly, chirality, and orientation of interfacial films by scanning tunneling microscopy. *Acc Chem Res.* 2000;33(7):491–501.
34. Shi DX, Ji W, Lin X, He XB, Lian JC, Gao L, et al. Role of lateral alkyl chains in modulation of molecular structures on metal surfaces. *Phys Rev Lett.* 2006;96(22):226101.
35. Cun H, Wang Y, du S, Zhang L, Zhang L, Yang B, et al. Tuning structural and mechanical properties of two-dimensional molecular crystals: the roles of carbon side chains. *Nano Lett.* 2012;12(3):1229–34.
36. Cai Z-F, Zhan G, Daukiya L, Eyley S, Thielemans W, Severin K, et al. Electric-field-mediated reversible transformation between supramolecular networks and covalent organic frameworks. *J Am Chem Soc.* 2019;141(29):11404–8.
37. Jiang N, Zhang YY, Liu Q, Cheng ZH, Deng ZT, du SX, et al. Diffusivity control in molecule-on-metal systems using electric fields. *Nano Lett.* 2010;10(4):1184–8.
38. Sagebiel S, Stricker L, Engel S, Ravoo BJ. Self-assembly of colloidal molecules that respond to light and a magnetic field. *Chem Commun.* 2017;53(67):9296–9.
39. Čížmár T, Romero LCD, Dholakia K, Andrews DL. Multiple optical trapping and binding: new routes to self-assembly. *J Phys B.* 2010; 43(10):102001.
40. Dai H-L, Geng YF, Zeng QD, Wang C. Photo-regulation of 2D supramolecular self-assembly: on-surface photochemistry studied by STM. *Chin Chem Lett.* 2017;28(4):729–37.
41. Song Y, Wang Y, Jin Q, Zhou K, Shi Z, Liu PN, et al. Self-assembly and local manipulation of Au-pyridyl coordination networks on metal surfaces. *ChemPhysChem.* 2017;18(15):2088–93.
42. Matvija P, Rozbořil F, Sobotík P, Ošťádal I, Pieczyrak B, Jurczyszyn L, et al. Electric-field-controlled phase transition in a 2D molecular layer. *Sci Rep.* 2017;7(1):7357.
43. Qi J, Gao Y, Jia H, Richter M, Huang L, Cao Y, et al. Force-activated isomerization of a single molecule. *J Am Chem Soc.* 2020;142(24): 10673–80.
44. Heyd J, Scuseria GE. Efficient hybrid density functional calculations in solids: assessment of the Heyd-Scuseria-Ernzerhof screened Coulomb hybrid functional. *J Chem Phys.* 2004;121(3):1187–92.
45. Heyd J, Scuseria GE, Ernzerhof M. Hybrid functionals based on a screened Coulomb potential. *J Chem Phys.* 2003;118(18):8207–15.
46. Krukau AV, Vydrov OA, Izmaylov AF, Scuseria GE. Influence of the exchange screening parameter on the performance of screened hybrid functionals. *J Chem Phys.* 2006;125(22):224106.
47. Becke AD. Density-functional thermochemistry. III. The role of exact exchange. *J Chem Phys.* 1993;98(7):5648–52.
48. Perdew JP, Ernzerhof M, Burke K. Rationale for mixing exact exchange with density functional approximations. *J Chem Phys.* 1996; 105(22):9982–5.
49. Grimme S. Semiempirical GGA-type density functional constructed with a long-range dispersion correction. *J Comput Chem.* 2006; 27(15):1787–99.
50. Grimme S, Antony J, Ehrlich S, Krieg H. A consistent and accurate ab initio parametrization of density functional dispersion correction (DFT-D) for the 94 elements H-Pu. *J Chem Phys.* 2010;132(15):154104.
51. Dion M, Rydberg H, Schröder E, Langreth DC, Lundqvist BI. Van der Waals density functional for general geometries. *Phys Rev Lett.* 2004;92(24):246401.
52. Lee K, Murray ÉD, Kong L, Lundqvist BI, Langreth DC. Higher-accuracy van der Waals density functional. *Phys Rev B.* 2010;82(8): 081101.

53. International roadmap for devices and systems 2020 edition. 2020. Available from: <https://irds.ieee.org/editions/2020>
54. Bilić A, Reimers JR, Hush NS. Adsorption of pyridine on the gold(111) surface: implications for “alligator clips” for molecular wires. *J Phys Chem B*. 2002;106(26):6740–7.
55. Bengone O, Alouani M, Blöchl P, Hugel J. Implementation of the projector augmented-wave LDA+U method: application to the electronic structure of NiO. *Phys Rev B*. 2000;62(24):16392–401.
56. Dil H, Lobo-Checa J, Laskowski R, Blaha P, Berner S, Osterwalder J, et al. Surface trapping of atoms and molecules with dipole rings. *Science*. 2008;319(5871):1824–6.
57. Ren J, Bao DL, Dong L, Gao L, Wu R, Yan L, et al. Lattice-directed construction of metal–organic molecular wires of pentacene on the Au(110) surface. *J Phys Chem C*. 2017;121(39):21650–7.
58. du SX, Gao HJ, Seidel C, Tsetseris L, Ji W, Kopf H, et al. Selective nontemplated adsorption of organic molecules on nanofacets and the role of bonding patterns. *Phys Rev Lett*. 2006;97(15):156105.
59. Barth JV, Weckesser J, Trimarchi G, Vladimirova M, de Vita A, Cai C, et al. Stereochemical effects in supramolecular self-assembly at surfaces: 1-D versus 2-D enantiomorphic ordering for PVBA and PEBA on Ag(111). *J Am Chem Soc*. 2002;124(27):7991–8000.
60. Marschall M, Reichert J, Weber-Bargioni A, Seufert K, Auwärter W, Klyatskaya S, et al. Random two-dimensional string networks based on divergent coordination assembly. *Nat Chem*. 2010;2:131–7.
61. Yang B, Wang Y, Cun H, du S, Xu M, Wang Y, et al. Direct observation of enantiospecific substitution in a two-dimensional chiral phase transition. *J Am Chem Soc*. 2010;132:10440–4.
62. Åhlund J, Schnadt J, Nilson K, Göthelid E, Schiessling J, Besenbacher F, et al. The adsorption of iron phthalocyanine on graphite: a scanning tunnelling microscopy study. *Surf Sci*. 2007;601(17):3661–7.
63. Zhang HG, Sun JT, Low T, Zhang LZ, Pan Y, Liu Q, et al. Assembly of iron phthalocyanine and pentacene molecules on a graphene monolayer grown on Ru(0001). *Phys Rev B*. 2011;84:245436.
64. Cheng ZH, Gao L, Deng ZT, Jiang N, Liu Q, Shi DX, et al. Adsorption behavior of iron phthalocyanine on Au(111) surface at sub-monolayer coverage. *J Phys Chem C*. 2007;111:9240–4.
65. Zhang YY, Du SX, Gao HJ. Binding configuration, electronic structure, and magnetic properties of metal phthalocyanines on a Au(111) surface studied with ab initio calculations. *Phys Rev B*. 2011;84(12):125446.
66. Petraki F, Peisert H, Aygül U, Latteyer F, Uihlein J, Vollmer A, et al. Electronic structure of FePc and interface properties on Ag(111) and Au(100). *J Phys Chem C*. 2012;116(20):11110–6.
67. Palmgren P, Yu S, Hennies F, Nilson K, Åkermark B, Göthelid M. Changing adsorption mode of FePc on TiO₂(110) by surface modification with bipyridine. *J Chem Phys*. 2008;129(7):074707.
68. Sun JT, Gao L, He XB, Cheng ZH, Deng ZT, Lin X, et al. Surface reconstruction transition of metals induced by molecular adsorption. *Phys Rev B*. 2011;83(11):115419.
69. Wu Q, Hu Z, Wang X, Chen Y, Lu Y. Synthesis and optical characterization of aluminum nitride nanobelts. *J Phys Chem B*. 2003;107(36):9726–9.
70. Urbani M, Ragoussi ME, Nazeeruddin MK, Torres T. Phthalocyanines for dye-sensitized solar cells. *Coord Chem Rev*. 2019;381:1–64.
71. Gao L, Liu Q, Zhang YY, Jiang N, Zhang HG, Cheng ZH, et al. Constructing an array of anchored single-molecule rotors on gold surfaces. *Phys Rev Lett*. 2008;101(19):197209.
72. Wu SW, Nazin GV, Chen X, Qiu XH, Ho W. Control of relative tunneling rates in single molecule bipolar electron transport. *Phys Rev Lett*. 2004;93(23):236802.
73. Ji W, Lu ZY, Gao H. Electron core–hole interaction and its induced ionic structural relaxation in molecular systems under x-ray irradiation. *Phys Rev Lett*. 2006;97(24):246101.
74. Liu Q, Zhang YY, Jiang N, Zhang HG, Gao L, du SX, et al. Identifying multiple configurations of complex molecules in dynamical processes: time resolved tunneling spectroscopy and density functional theory calculation. *Phys Rev Lett*. 2010;104(16):166101.
75. Huan Q, Jiang Y, Zhang YY, Ham U, Ho W. Spatial imaging of individual vibronic states in the interior of single molecules. *J Chem Phys*. 2011;135(1):014705.
76. Zhao A, Hu Z, Wang B, Xiao X, Yang J, Hou JG. Kondo effect in single cobalt phthalocyanine molecules adsorbed on Au(111) monoatomic steps. *J Chem Phys*. 2008;128(23):234705.
77. Cheng ZH, Gao L, Deng ZT, Liu Q, Jiang N, Lin X, et al. Epitaxial growth of iron phthalocyanine at the initial stage on Au(111) surface. *J Phys Chem C*. 2007;111:2656–60.
78. Liu L, Yang K, Jiang Y, Song B, Xiao W, Li L, et al. Reversible single spin control of individual magnetic molecule by hydrogen atom adsorption. *Sci Rep*. 2013;3:1210.
79. Deng Z, Guo HM, Guo W, Gao L, Cheng ZH, Shi DX, et al. Structural properties of tetra-tert-butyl zinc(II) phthalocyanine isomers on a Au(111) surface. *J Phys Chem C*. 2009;113:11223–7.
80. Zhang L, Cheng Z, Huan Q, He X, Lin X, Gao L, et al. Site- and configuration-selective anchoring of iron–phthalocyanine on the step edges of Au(111) surface. *J Phys Chem C*. 2011;115(21):10791–6.
81. Wang Y, Ge X, Schull G, Berndt R, Bornholdt C, Koehler F, et al. Azo supramolecules on Au(111) with controlled size and shape. *J Am Chem Soc*. 2008;130(13):4218–9.
82. Zhang X, Tang L, Guo Q. Low-temperature growth of C60 monolayers on Au(111): island orientation control with site-selective nucleation. *J Phys Chem C*. 2010;114(14):6433–9.

83. Liu LW, Yang K, Xiao WD, Jiang YH, Song BQ, du SX, et al. Selective adsorption of metal-phthalocyanine on Au(111) surface with hydrogen atoms. *Appl Phys Lett*. 2013;103:023110.
84. Gao L, Ji W, Hu YB, Cheng ZH, Deng ZT, Liu Q, et al. Site-specific Kondo effect at ambient temperatures in iron-based molecules. *Phys Rev Lett*. 2007;99(10):106402.
85. Bogani L, Wernsdorfer W. Molecular spintronics using single-molecule magnets. *Nat Mater*. 2008;7(3):179–86.
86. Sanvito S. Molecular spintronics. *Chem Soc Rev*. 2011;40(6):3336–55.
87. Aradhya SV, Venkataraman L. Single-molecule junctions beyond electronic transport. *Nat Nanotechnol*. 2013;8(6):399–410.
88. Marsman M, Paier J, Stroppa A, Kresse G. Hybrid functionals applied to extended systems. *J Phys Condens Matter*. 2008;20(6):064201.
89. Maslyuk VV, Aristov VY, Molodtsova OV, Vyalikh DV, Zhilin VM, Ossipyan YA, et al. The electronic structure of cobalt phthalocyanine. *Appl Phys A*. 2009;94(3):485–9.
90. Hu Z, Li B, Zhao A, Yang J, Hou JG. Electronic and magnetic properties of metal phthalocyanines on Au(111) surface: a first-principles study. *J Phys Chem C*. 2008;112(35):13650–5.
91. Berland K, Einstein TL, Hyldgaard P. Rings sliding on a honeycomb network: adsorption contours, interactions, and assembly of benzene on Cu(111). *Phys Rev B*. 2009;80(15):155431.
92. Li S, Hao J, Li F, Niu Z, Hu Z, Zhang L. The key role of van der Waals interactions in MPc/Au(111) ($M = \text{Co, Fe, H}_2$) systems based on first-principles calculations. *J Phys Chem C*. 2014;118(48):27843–9.
93. Toyoda K, Nakano Y, Hamada I, Lee K, Yanagisawa S, Morikawa Y. First-principles study of the pentacene/Cu(111) interface: adsorption states and vacuum level shifts. *J Electron Spectrosc Relat Phenom*. 2009;174(1):78–84.
94. Zhao A, Li Q, Chen L, Xiang H, Wang W, Pan S, et al. Controlling the Kondo effect of an adsorbed magnetic ion through its chemical bonding. *Science*. 2005;309(5740):1542–4.
95. Iancu V, Deshpande A, Hla S-W. Manipulating Kondo temperature via single molecule switching. *Nano Lett*. 2006;6(4):820.
96. Liu L, Yang K, Jiang Y, Song B, Xiao W, Song S, et al. Revealing the atomic site-dependent g factor within a single magnetic molecule via the extended Kondo effect. *Phys Rev Lett*. 2015;114(12):126601.
97. Guo X, Zhu Q, Zhou L, Yu W, Lu W, Liang W. Evolution and universality of two-stage Kondo effect in single manganese phthalocyanine molecule transistors. *Nat Commun*. 2021;12(1):1566.
98. Fu Y-S, Ji SH, Chen X, Ma XC, Wu R, Wang CC, et al. Manipulating the Kondo resonance through quantum size effects. *Phys Rev Lett*. 2007;99(25):256601.
99. Warner B, el Hallak F, Prüser H, Sharp J, Persson M, Fisher AJ, et al. Tunable magnetoresistance in an asymmetrically coupled single-molecule junction. *Nat Nanotechnol*. 2015;10(3):259–63.
100. Roch N, Florens S, Bouchiat V, Wernsdorfer W, Balestro F. Quantum phase transition in a single-molecule quantum dot. *Nature*. 2008;453(7195):633–7.
101. Yang K, Chen H, Pope T, Hu Y, Liu L, Wang D, et al. Tunable giant magnetoresistance in a single-molecule junction. *Nat Commun*. 2019;10(1):3599.
102. Kügel J, Karolak M, Krönlein A, Senkpiel J, Hsu PJ, Sangiovanni G, et al. State identification and tunable Kondo effect of MnPc on Ag(001). *Phys Rev B*. 2015;91(23):235130.
103. Hatter N, Heinrich BW, Rolf D, Franke KJ. Scaling of Yu-Shiba-Rusinov energies in the weak-coupling Kondo regime. *Nat Commun*. 2017;8(1):2016–6.
104. Fu Y-S, Xue Q-K, Wiesendanger R. Spin-resolved splitting of Kondo resonances in the presence of RKKY-type coupling. *Phys Rev Lett*. 2012;108(8):087203.
105. Franke KJ, Schulze G, Pascual JI. Competition of superconducting phenomena and Kondo screening at the nanoscale. *Science*. 2011;332(6032):940–4.
106. Mugarza A, Krull C, Robles R, Stepanow S, Ceballos G, Gambardella P. Spin coupling and relaxation inside molecule–metal contacts. *Nat Commun*. 2011;2(1):490.
107. Mugarza A, Robles R, Krull C, Korytár R, Lorente N, Gambardella P. Electronic and magnetic properties of molecule-metal interfaces: transition-metal phthalocyanines adsorbed on Ag(100). *Phys Rev B*. 2012;85(15):155437.
108. Nguyen TQ, Escaño MCS, Kasai H. Nitric oxide adsorption effects on metal phthalocyanines. *J Phys Chem B*. 2010;114(31):10017–21.
109. Yang K, Liu L, Zhang L, Xiao W, Fei X, Chen H, et al. Reversible achiral-to-chiral switching of single Mn–phthalocyanine molecules by thermal hydrogenation and inelastic electron tunneling dehydrogenation. *ACS Nano*. 2014;8:2246–51.
110. Yang K, Xiao W, Liu L, Fei X, Chen H, du S, et al. Construction of two-dimensional hydrogen clusters on Au(111) directed by phthalocyanine molecules. *Nano Res*. 2013;7(1):79–84.
111. Tao L, Guo W, Zhang YY, Zhang YF, Sun J, du S, et al. Quantum nutcracker for near-room-temperature H_2 dissociation. *Sci Bull*. 2019;64(1):4–7.
112. Park JH, Choudhury P, Kummel AC. NO adsorption on copper phthalocyanine functionalized graphite. *J Phys Chem C*. 2014;118(19):10076–82.
113. Stróżecka A, Soriano M, Pascual JI, Palacios JJ. Reversible change of the spin state in a manganese phthalocyanine by coordination of CO molecule. *Phys Rev Lett*. 2012;109(14):147202.
114. Sedona F, di Marino M, Forrer D, Vittadini A, Casarin M, Cossaro A, et al. Tuning the catalytic activity of Ag(110)-supported Fe phthalocyanine in the oxygen reduction reaction. *Nat Mater*. 2012;11(11):970–7.
115. Ling Q-D, Liaw DJ, Teo EYH, Zhu C, Chan DSH, Kang ET, et al. Polymer memories: bistable electrical switching and device performance. *Polymer*. 2007;48(18):5182–201.

116. Ling Q-D, Liaw DJ, Zhu C, Chan DSH, Kang ET, Neoh KG. Polymer electronic memories: materials, devices and mechanisms. *Prog Polym Sci.* 2008;33(10):917–78.
117. Ling Q-D, Song Y, Lim SL, Teo EYH, Tan YP, Zhu C, et al. A dynamic random access memory based on a conjugated copolymer containing electron-donor and -acceptor moieties. *Angew Chem Int Ed.* 2006;45(18):2947–51.
118. Ling Q-D, Chang FC, Song Y, Zhu CX, Liaw DJ, Chan DSH, et al. Synthesis and dynamic random access memory behavior of a functional polyimide. *J Am Chem Soc.* 2006;128(27):8732–3.
119. Lim SL, Li NJ, Lu JM, Ling QD, Zhu CX, Kang ET, et al. Conductivity switching and electronic memory effect in polymers with pendant azobenzene chromophores. *ACS Appl Mater Interfaces.* 2009;1(1):60–71.
120. Li H, Jin Z, Li N, Xu Q, Gu H, Lu J, et al. A small-molecule-based device for data storage and electro-optical switch applications. *J Mater Chem.* 2011;21(16):5860–2.
121. Zhang Y, Zhang Y, Li G, Lu J, Lin X, Tan Y, et al. Construction of single-crystalline supramolecular networks of perchlorinated hexaperi-hexabenzocoronene on Au(111). *J Chem Phys.* 2015;142(10):101911.
122. Zhou H, Liu J, du S, Zhang L, Li G, Zhang Y, et al. Direct visualization of surface-assisted two-dimensional diyne polycyclotrimerization. *J Am Chem Soc.* 2014;136(15):5567–70.
123. Liu J, Ruffieux P, Feng X, Müllen K, Fasel R. Cyclotrimerization of arylalkynes on Au(111). *Chem Commun.* 2014;50(76):11200–3.
124. Dai J, Fan Q, Wang T, Kuttner J, Hilt G, Gottfried JM, et al. The role of the substrate structure in the on-surface synthesis of organometallic and covalent oligophenylene chains. *Phys Chem Chem Phys.* 2016;18(30):20627–34.
125. Huang Z, Dong G. Site-selectivity control in organic reactions: a quest to differentiate reactivity among the same kind of functional groups. *Acc Chem Res.* 2017;50(3):465–71.
126. Zhong Q, Ebeling D, Tschakert J, Gao Y, Bao D, du S, et al. Symmetry breakdown of 4,4''-diamino-p-terphenyl on a Cu(111) surface by lattice mismatch. *Nat Commun.* 2018;9(1):3277.
127. Khsar KR, Schwartz DK, Medlin JW. Control of metal catalyst selectivity through specific noncovalent molecular interactions. *J Am Chem Soc.* 2014;136(1):520–6.
128. Toste FD, Sigman MS, Miller SJ. Pursuit of noncovalent interactions for strategic site-selective catalysis. *Acc Chem Res.* 2017;50(3):609–15.
129. Zhou X, Bebensee F, Yang M, Bebensee R, Cheng F, He Y, et al. Steering surface reaction at specific sites with self-assembly strategy. *ACS Nano.* 2017;11(9):9397–404.
130. Xing L, Peng Z, Li W, Wu K. On controllability and applicability of surface molecular self-assemblies. *Acc Chem Res.* 2019;52(4):1048–58.
131. Henkelman G, Uberuaga BP, Jonsson H. A climbing image nudged elastic band method for finding saddle points and minimum energy paths. *J Chem Phys.* 2000;113:9901–4.
132. Yuan D, Liao H, Hu W. Assessment of van der Waals inclusive density functional theory methods for adsorption and selective dehydrogenation of formic acid on Pt(111) surface. *Phys Chem Chem Phys.* 2019;21(37):21049–56.
133. Steinmann SN, Corminboeuf C. A generalized-gradient approximation exchange hole model for dispersion coefficients. *J Chem Phys.* 2011;134(4):044117.
134. Steinmann SN, Corminboeuf C. Comprehensive benchmarking of a density-dependent dispersion correction. *J Chem Theory Comput.* 2011;7(11):3567–77.
135. Klimeš J, Bowler DR, Michaelides A. Chemical accuracy for the van der Waals density functional. *J Phys Condens Matter.* 2009;22(2):022201.
136. Meng G, Sun J, Tao L, Ji K, Wang P, Wang Y, et al. Ru₁Co_n single-atom alloy for enhancing Fischer–Tropsch synthesis. *ACS Catal.* 2021;11(3):1886–96.
137. de Oteyza DG, Barrera E, Dosch H, Ortega JE, Wakayama Y. Tunable symmetry and periodicity in binary supramolecular nanostructures. *Phys Chem Chem Phys.* 2011;13(10):4220–3.
138. Dalvit C, Vulpetti A. Weak intermolecular hydrogen bonds with fluorine: detection and implications for enzymatic/chemical reactions, chemical properties, and ligand/protein fluorine NMR screening. *Chem Eur J.* 2016;22(22):7592–601.
139. Chen Q, Cramer JR, Liu J, Jin X, Liao P, Shao X, et al. Steering on-surface reactions by a self-assembly approach. *Angew Chem Int Ed.* 2017;56(18):5026–30.
140. Wiengarten A, Lloyd JA, Seufert K, Reichert J, Auwärter W, Han R, et al. Surface-assisted cyclodehydrogenation; break the symmetry, enhance the selectivity. *Chemistry.* 2015;21(35):12285–90.
141. Chen H, Tao L, Wang D, Wu ZY, Zhang JL, Gao S, et al. Stereoselective on-surface cyclodehydrofluorization of a tetraphenylporphyrin and homochiral self-assembly. *Angew Chem Int Ed Engl.* 2020;59(40):17413–6.
142. Buchner F, Kellner I, Hieringer W, Görling A, Steinrück HP, Marbach H. Ordering aspects and intramolecular conformation of tetraphenylporphyrins on Ag(111). *Phys Chem Chem Phys.* 2010;12(40):13082–90.
143. Chen H, Pope T, Wu ZY, Wang D, Tao L, Bao DL, et al. Evidence for ultralow-energy vibrations in large organic molecules. *Nano Lett.* 2017;17(8):4929–33.
144. Röckert M, Ditze S, Stark M, Xiao J, Steinrück HP, Marbach H, et al. Abrupt coverage-induced enhancement of the self-metalation of tetraphenylporphyrin with Cu(111). *J Phys Chem C.* 2014;118(3):1661–7.
145. Nørskov JK, Bligaard T, Logadottir A, Bahn S, Hansen LB, Bollinger M, et al. Universality in heterogeneous catalysis. *J Catal.* 2002;209(2):275–8.

146. Tao L, Zhang YY, Pantelides ST, du S. Tuning the catalytic activity of a quantum nutcracker for hydrogen dissociation. *Surfaces*. 2020; 3(1):40–7.
147. Hammer B, Norskov JK. Why gold is the noblest of all the metals. *Nature*. 1995;376:238–40.
148. Wijzenbroek M, Helstone D, Meyer J, Kroes GJ. Dynamics of H₂ dissociation on the close-packed (111) surface of the noblest metal: H₂ + Au(111). *J Chem Phys*. 2016;145(14):144701–13.
149. Tierney HL, Baber AE, Kitchin JR, Sykes ECH. Hydrogen dissociation and spillover on individual isolated palladium atoms. *Phys Rev Lett*. 2009;103(24):246102.
150. Haruta M, Daté M. Advances in the catalysis of Au nanoparticles. *Appl Catal A Gen*. 2001;222(1–2):427–37.
151. Zhao M, Wang A, Zhang X. Half-metallicity of a Kagome spin lattice: the case of a manganese bis-dithiolene monolayer. *Nanoscale*. 2013;5(21):10404–8.
152. Zhang X, Zhao M. Robust half-metallicity and topological aspects in two-dimensional Cu-TPyB. *Sci Rep*. 2015;5(1):14098.
153. Jin Y, Chen Z, Xia B, Zhao Y, Wang R, Xu H. Large-gap quantum anomalous Hall phase in hexagonal organometallic frameworks. *Phys Rev B*. 2018;98(24):245127.
154. Yamada MG, Fujita H, Oshikawa M. Designing Kitaev spin liquids in metal–organic frameworks. *Phys Rev Lett*. 2017;119(5):057202.
155. Huang X, Sheng P, Tu Z, Zhang F, Wang J, Geng H, et al. A two-dimensional π - d conjugated coordination polymer with extremely high electrical conductivity and ambipolar transport behaviour. *Nat Commun*. 2015;6(1):7408.
156. Zhang X, Zhou Y, Cui B, Zhao M, Liu F. Theoretical discovery of a superconducting two-dimensional metal–organic framework. *Nano Lett*. 2017;17(10):6166–70.
157. Huang X, Zhang S, Liu L, Yu L, Chen G, Xu W, et al. Superconductivity in a copper(II)-based coordination polymer with perfect Kagome structure. *Angew Chem Int Ed Engl*. 2018;57(1):146–50.
158. Wang ZF, Su N, Liu F. Prediction of a two-dimensional organic topological insulator. *Nano Lett*. 2013;13(6):2842–5.
159. Silveira OJ, Lima ÉN, Chacham H. Bilayers of Ni₃C₁₂S₁₂ and Pt₃C₁₂S₁₂: graphene-like 2D topological insulators tunable by electric fields. *J Phys Condens Matter*. 2017;29(46):465502.
160. Mostofi AA, Yates JR, Lee YS, Souza I, Vanderbilt D, Marzari N. wannier90: a tool for obtaining maximally-localised Wannier functions. *Comput Phys Commun*. 2008;178(9):685–99.
161. Sancho MPL, Sancho JML, Sancho JML, Rubio J. Highly convergent schemes for the calculation of bulk and surface Green functions. *J Phys F*. 1985;15(4):851–8.
162. Wang ZF, Liu Z, Liu F. Quantum anomalous Hall effect in 2D organic topological insulators. *Phys Rev Lett*. 2013;110(19):196801.
163. Wang ZF, Liu Z, Liu F. Organic topological insulators in organometallic lattices. *Nat Commun*. 2013;4:1471.
164. Zhou Q, Wang J, Chwee TS, Wu G, Wang X, Ye Q, et al. Topological insulators based on 2D shape-persistent organic ligand complexes. *Nanoscale*. 2015;7(2):727–35.
165. Zhao B, Zhang J, Feng W, Yao Y, Yang Z. Quantum spin Hall and Z₂ metallic states in an organic material. *Phys Rev B*. 2014;90(20):201403.
166. Kambe T, Sakamoto R, Hoshiko K, Takada K, Miyachi M, Ryu JH, et al. π -Conjugated nickel bis(dithiolene) complex nanosheet. *J Am Chem Soc*. 2013;135(7):2462–5.
167. Campbell MG, Sheberla D, Liu SF, Swager TM, Dincă M. Cu(3)(hexaiminotriphenylene)(2): an electrically conductive 2D metal-organic framework for chemiresistive sensing. *Angew Chem Int Ed Engl*. 2015;54(14):4349–52.
168. Gao Y, Zhang YY, Sun JT, Zhang L, Zhang S, du S. Quantum anomalous Hall effect in two-dimensional Cu-dicyanobenzene coloring-triangle lattice. *Nano Res*. 2020;13(6):1571–5.
169. Zhang LZ, Wang ZF, Huang B, Cui B, Wang Z, du SX, et al. Intrinsic two-dimensional organic topological insulators in metal-dicyanoanthracene lattices. *Nano Lett*. 2016;16(3):2072–5.
170. Zhang J, Shchyrba A, Nowakowska S, Meyer E, Jung TA, Muntwiler M. Probing the spatial and momentum distribution of confined surface states in a metal coordination network. *Chem Commun (Camb)*. 2014;50(82):12289–92.
171. Yan L, Silveira OJ, Alldritt B, Krejčí O, Foster AS, Liljeroth P. Synthesis and local probe gating of a monolayer metal-organic framework. *Adv Funct Mater*. 2021;31(22):2100519.
172. Song Y, Pan J, Zhang YF, Yang H, du S. Monolayer iridium sulfide halides with high mobility transport anisotropy and highly efficient light harvesting. *J Phys Chem Lett*. 2021;12(25):6007–13.
173. Zhang Y-F, Pan J, Banjade H, Yu J, Lin H, Bansil A, et al. Two-dimensional MX Dirac materials and quantum spin Hall insulators with tunable electronic and topological properties. *Nano Res*. 2021;14(3):584–9.
174. Zhou Q, Tang P, Liu S, Pan J, Yan Q, Zhang SC. Learning atoms for materials discovery. *Proc Natl Acad Sci U S A*. 2018;115(28):E6411–7.
175. Liu Z-Y, Pan J-B, Zhang Y-Y, Du S-X. First principles calculation of two-dimensional materials at an atomic scale. *Acta Phys Sin*. 2021; 70(2):027301.

How to cite this article: Tao L, Zhang Y, Du S. Structures and electronic properties of functional molecules on metal substrates: From single molecule to self-assemblies. *WIREs Comput Mol Sci*. 2021;e1591. <https://doi.org/10.1002/wcms.1591>